Density and size-dependent bioturbation effects of the infaunal polychaete Nephtys incisa on sediment biogeochemistry and solute exchange

Emma Michaud, Robert Aller, Qingzhi Zhu, Christina Heilbrun, Georges Stora

Journal of Marine Research, 79, 181–220, 2021

Density and size-dependent bioturbation effects of the infaunal polychaete *Nephtys incisa* on sediment biogeochemistry and solute exchange

by Emma Michaud[1,2,3], Robert C. Aller[2], Qingzhi Zhu[2], Christina Heilbrun[2], and Georges Stora[4]

ABSTRACT

The impact of bioturbation on the geochemistry of aquatic sediments is known to depend on the benthic infauna species that are present. However, burrowing and activity patterns of each species may also change during the different stages of a life cycle. In this study, we examined the effects of four size classes of the polychaete *Nephtys incisa* on burrow networks and sediment biogeochemistry. In our experimental aquaria, the total biovolume (∼biomass) of *Nephtys* was kept constant, but different age classes were introduced, so the size and abundance varied between treatments. Despite differences in the geometry of burrow networks (due to varying density and size of burrows as revealed by X-radiography), the transport of nonreactive solutes (Br^-) showed little difference between treatments. In contrast, the depth distribution of reactive solutes (Fe^{2+}, Mn^{2+}, TPO_4^{3-}, TCO_2, O_2, pH) depended on oxidized sediment volumes and on spatial micro-heterogeneity related to burrowing patterns. Net fluxes of O_2, TCO_2, and NO_3^- fluxes were strongly affected by age-dependent burrowing patterns. Carbonate dissolution and remineralization rates (reflected by TCO_2 fluxes) were enhanced as the size of individuals increased. NO_3^- fluxes showed progressive change from dominance of nitrification (release) to denitrification (uptake) as burrow densities decreased with larger individuals. We conclude that different age-size classes of a single species at identical biovolume affect biogeochemical cycling differently, due to changes in burrow sizes and burrow densities. Because of redox reaction coupling associated with burrow geometries (Fe^{2+}, Mn^{2+} oxidation patterns), similar magnitudes of nonlocal transport may be a misleading indicator of biogenic impacts. Our observations demonstrate that biogeochemical impacts must be evaluated in the context of size (age-) specific traits and population densities rather than biomass or biovolume alone.

Keywords: benthic fluxes, bioirrigation, burrow geometry, carbonate dissolution, diagenetic models, planar optodes, respiration

1. Université de Brest, CNRS, IRD, Ifremer, LEMAR, F-29280 Plouzané, France; orcid: 0000-0002-7304-4069
2. School of Marine and Atmospheric Sciences, Stony Brook, NY 11794-5000, USA; orcid: 0000-0003-4360-8406, orcid: 0000-0003-2496-6718, orcid: 0000-0002-1210-3205
3. Corresponding author: ***e-mail: Emma.Michaud@univ-brest.fr***
4. Aix Marseille Université, MIO Institut Méditerranéen d'Océanologie, CNRS, F-13288 Marseille Cedex 9, France; orcid: 0000-0001-8872-8124

Supplemental materials for this article are available online.

1. Introduction

Bioturbation has a major effect on organic matter remineralization, nutrient regeneration, and elemental fluxes in the seabed (Aller 1982, 2001; Quintana et al. 2015) and has played an essential role in marine biogeochemical cycling since the evolution of metazoan life (Thayer 1979; Meysman, Middelburg, and Heip 2006; Canfield and Farquhar 2009; Buatois et al. 2018). Rather than species diversity or species biomass per se, particular species are critical in determining the impact of bioturbation on physical properties and sediment geochemistry (Rhoads 1974). The relationships of such key species to benthic respiration and mineralization intensity have been examined both in situ and ex situ (Mermillod-Blondin et al. 2004; Norling et al. 2007; D'Andrea and DeWitt 2009; Braeckman et al. 2014). Bioirrigation and burrow ventilation patterns, particle reworking rates, tube construction activity, organism mobility, and population densities are general factors that determine the impact of particular species on sedimentary biogeochemical cycling and fluxes (Marinelli and Williams 2003; Kristensen and Kostka 2005; Michaud et al. 2005; Braeckman et al. 2014). Inter- and intraspecific interactions can also influence bioturbation activity, and in this way either facilitate or inhibit animal–sediment interactions that affect nutrient cycling (Mermillod-Blondin et al. 2004; Norling et al. 2007; Michaud et al. 2009).

From a mechanistic standpoint, multiple properties of burrow structures and biogenic microenvironments determine the impact of benthos on sedimentary biogeochemical reactions. These properties include burrow diameter and length (burrow wall surface area), burrow or microenvironment persistence (temporal stability), ventilation frequency (interior boundary conditions), burrow wall composition, and the depth and spatial organization of burrows in a deposit (Aller 1982, 2001; Kristensen and Kostka 2005; Meysman et al. 2010; Dornhoffer, Waldbusser, and Meile 2012; Pischedda et al. 2012). Burrow properties influence the kinetics of specific biogeochemical reactions, thus influencing concentration patterns and sediment–water fluxes (Marinelli 1992; Aller 2001; Gilbert, Aller, and Hulth 2003; Waldbusser et al. 2004; Waldbusser and Marinelli 2006; Michaud, Aller, and Stora 2010). Individuals from the same species can modify their burrow morphology as a function of sediment type or sedimentary reactivity (Katrak, Dittmann, and Seuront 2008; Needham et al. 2010).

The population densities of infauna can also affect the properties of burrows (Heilskov and Holmer 2001; Marinelli and Williams 2003; D'Andrea and DeWitt 2009; Dunn et al. 2009; Braeckman et al. 2010; De Backer et al. 2011; Murray, Douglas, and Solan 2014). In addition, burrowing and activity patterns may change during the different stages of a species's life cycle. For example, adult animals are larger and build deeper burrows than younger animals (Whitlatch 1976; Chan, Chan, and Leung 2006), and juveniles often occur at higher densities and may have different activity patterns than adults. To our knowledge, the effects of such age–size distributions on sedimentary biogeochemical processes have not been experimentally investigated as such, although diagenetic model calculations allow inference of potential impacts of transport scaling on reactive and non-reactive solutes (Aller 1982, 1988; Meile et al. 2005; Michaud, Aller, and Stora 2010). The main

question of the present study was therefore: Can different burrow scaling and burrowing behavior between adults and juveniles of the same species at similar biomass differentially affect biogeochemical reaction patterns? To address this question, we examined the effects of four discrete size classes of the polychaete *Nephtys incisa* on burrow geometries, on sedimentary solute profiles, and on biogeochemical fluxes associated with organic matter remineralization.

The evaluation of the impact of faunal size on sediment biogeochemistry requires some form of normalization, and typically activities or effects are normalized relative to quantities such as biomass or numerical abundance (Emmerson and Raffaelli 2000; Mermillod-Blondin et al. 2004; Solan et al. 2004; Norling et al. 2007; Braeckman et al. 2014; Hale et al. 2014; Kauppi et al. 2018). In the case of particle reworking by benthos, Gilbert et al. (2007) found that the biovolume of infauna was linearly related to the quantity of sediment that infauna displaced during burrowing and feeding. Biovolume can also be directly related to burrow geometries and species-specific biogenic properties that couple to solute transport, and can affect biological interactions such as competition for space (Michaud et al. 2009). Normalization to constant biovolume is therefore a reasonable functional basis by which to evaluate the impact of benthos on sedimentary biogeochemical processes. In the present experiments, we have adjusted population densities of different sized individuals to the same total biovolume in all experimental treatments. Note that in our case, the normalization to biovolume and biomass are similar because the mass density of the studied species, *Nephtys incisa*, does not appreciably vary with age. We hypothesized that populations of adults and juveniles of the same species with the same biovolume can induce different burrowing patterns and geometrical scaling of burrow structures, and thus differentially affect benthic biogeochemical properties.

2. Material and methods

a. Sediment and faunal sampling

Sediment and animals were collected by grab sampling from the upper ∼15 cm of the seabed at a subtidal site in Smithtown Bay (15 m water depth, 40° 56.696′N, 73° 13.786′W), central Long Island Sound, USA, on 8 November 2007. Sediment deposits encountered were silty mud, the bottom water salinity at the time of sampling was 27, and the average organic carbon content was 2.31 ± 0.27%. Individual specimens of the polychaete *Nephtys incisa* were retrieved from the sediment and allocated to one of four size classes based on length and diameter (Table 1): Extra-Large (XL), Large (L), Medium (M), and Small (S).

These size classes correspond to specific age groups (Table 1) for the natural population of this region (Zajac and Whitlatch 1988). Animals from a given size class were kept in separate plastic containers with a thin layer of sediment (∼0.5–1 cm) overlain by continuously oxygenated seawater. Sediment and animals were subsequently held in the dark in a cold room at 15°C until further use.

Table 1. Individual worm parameters for each experimental aquarium: number, biomass (g), biovolume (mL), length (mm), and diameter (width in mm). Total biomass (g) and biovolume (mL) in each aquarium are also indicated.

Size class	Individual number	Mean individual biomass (g)	Mean individual biovolume (mL)	Mean individual length (mm)	Mean individual diameter (mm)	Total biomass (g)	Total biovolume (mL)	Specific age structure (years)
Tanks for burrow structure analysis								
XL	1	0.95	1.1	80	8	0.95	1.1	> 4
L	2	0.43 ± 0.01	0.5 ± 0.01	45	6	0.86 ± 0.02	1 ± 0.01	3.5
M	4	0.22 ± 0.01	0.25 ± 0.05	34 ± 2.5	4	0.89 ± 0.01	1 ± 0.05	2.5
S	8	0.10 ± 0.02	0.10 ± 0.06	17 ± 2.5	2	0.8 ± 0.02	1 ± 0.06	< 1
Tanks for biogeochemical studies								
XL	3	0.75 ± 0.18	0.96 ± 0.20	80 ± 10	8	2.25 ± 0.18	2.90 ± 0.20	> 4
L	6	0.40 ± 0.03	0.50 ± 0.08	48 ± 2.6	6	2.40 ± 0.03	3.00 ± 0.08	3.5
M	12	0.18 ± 0.05	0.25 ± 0.05	33 ± 2.6	4	2.00 ± 0.05	2.80 ± 0.05	2.5
S	24	0.09 ± 0.03	0.12 ± 0.05	17 ± 2.5	2	2.16 ± 0.05	2.80 ± 0.07	< 1

Notes: XL: aquarium containing extra large individuals; L: aquarium containing large individuals; M: aquarium containing medium individuals; S: aquarium containing small individuals. Each size class (last column) corresponds to a specific age structure based on Zajac and Whitlach (1988). Mean ± SD.

b. Experimental setup

During sediment collection, sediment cores were sectioned in separate depth intervals (0–2 cm; 2–4 cm; 4–6 cm; 6–10 cm; and 10–15 cm), and the sediment from a given interval was subsequently sieved without water to remove fauna (mesh size = 1 mm; procedure as in Michaud, Aller, and Stora [2010]). On 21 November (i.e., 13 days after collection), sediment was introduced into glass flat panel aquaria to a total depth of 15 cm, following the protocol of Michaud, Aller, and Stora (2010). The goal was to retain the natural pattern of the sediment organic matter reactivity (sequentially filling the aquaria with sediment from 10–15 cm; 6–10 cm; 4–6 cm; 2–4 cm; and 0–2 cm). Sediments in the aquaria were covered by 10 cm of overlying water (fresh, unfiltered seawater from Long Island Sound; water aeration and replacement are discussed below). Two series of aquaria were set up: A first series of six was dedicated for burrow network analysis (21 cm length, 3 cm width, 26 cm height), and another series of 12 for biogeochemical analysis (21 cm length, 9 cm width, 26 cm height), as summarized in supplemental file S1.

The burrow network experiment was started on 26 November and included five aquaria: one aquarium for each size class (i.e., XL, L, M, S) and one control without animals. The biogeochemical analysis experiment included 12 aquaria in total: two for each size class (i.e, XL, L, M, S) and four replicated controls without animals (C). Aquaria were given a code composed of the treatment (XL, L, M, S, C) and a group label (groups A, B, C, D), reflecting the date at which the sediment was introduced (sediment filling occurred on

four consecutive days for practical reasons). Start dates were: 21 November for XLA, LA, and CA; 22 November for XLB, MB, and CB; 23 November for LC, MC, and CC; 24 November for SD1, SD2, and CD. The entire biogeochemical series (12 aquaria) was used for measurements of solute fluxes across the sediment–water interface at approximately two-week intervals. For sediment composition analyses, one set of six aquaria (four with different size classes: XLA, LA, MB, SD2; two controls: CA, CB; all randomly selected) was used for destructive analysis after approximately one month, and the second set (XLB, LC, MC, SD1, CC, CD) was retained for destructive analysis at two months. The two-month time data are, however, not considered here because partial animal mortality compromised results.

At the starting date, *Nephtys* specimens were introduced into the aquaria and the abundances were adjusted to attain the same total biovolume in each aquarium ($\sim$3 mL). To this end, the biomass of individual specimens was measured before introduction into the aquaria, and the individual biovolume was calculated using a fixed mass density of 0.86 g mL^{-1}. The added densities corresponded to 3 XL, 6 L, 12 M, and 24 S individuals per aquarium in the biogeochemical series and 1 XL, 2 L, 4 M, and 8 S individuals per aquarium in the burrow network series (Table 1), corresponding to real densities of 214 ind m^{-2} (XL), 427 ind m^{-2} (L), 855 ind m^{-2} (M) and 1709 ind m^{-2} (S), which is well within the natural range (Zajac and Whitlatch 1988). The aquaria were placed in the dark, to prevent algal growth, and held at room temperature (22 ± 2°C) for one month. The aquaria for burrow network analysis were covered by a plastic sheet to inhibit evaporation, the overlying water was continuously aerated, and completely renewed every five days (Michaud, Aller, and Stora 2010). The aquaria for biogeochemical measurements were sealed with gasketed tops configured with luer lock penetrators, and were connected to individual secondary, aerated reservoirs (4L) through which water was continuously recirculated using a peristaltic pump ($\sim$10 mL min^{-1}). When sealed, aquaria enclosed an approximate volume of $1{,}200 \pm 47$ mL of overlying water (average of the eight aquaria), and so the residence time of water in the aquarium is $\sim$2 hours. At particular time points, the water circulation was temporarily stopped (by stopping the pump), which enabled closed incubations to determine the flux across the sediment–water interface (see below).

The water in each aerated reservoir was completely renewed every four days with fresh, unfiltered seawater from Long Island Sound. Each biogeochemical aquarium contained a suspended stirring bar, which was magnetically coupled to a small motor attached to the exterior of the top. The water was stirred continuously at $\sim$40–60 rpm.

c. Burrow structures analyses

X-radiography was applied to visualize and quantify the burrows inside the sediment every seven days over the first month, as described in Michaud, Aller, and Stora (2010). X-radiograph images were made binary (white = burrow, black = no burrow) for further quantitative analysis (Fig. 1a). Visible inspection of structures at the aquarium interface was

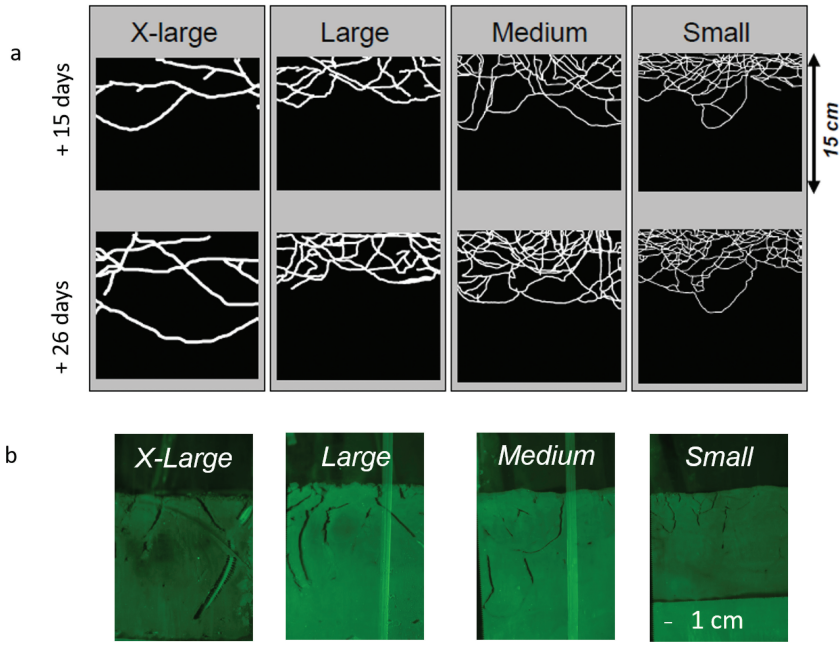

Figure 1. *Nephtys incisa* burrowing networks. (a) Binarized images obtained from X-radiograph analyses for each treatment: XL (Extra-Large), L (Large), M (Medium), S (Small) after 15 days and 26 days from the starting date. (b) Visible images (green spectral band) from aquaria showing the size and length of burrows present at the glass interface. One image for each size class of individuals (XL, L, M, S).

used to qualitatively confirm patterns revealed by X-radiography (Fig. 1b). Several quantities that characterize the burrow geometry were calculated from the binary X-radiograph images.

Mean burrow diameter $Ø_{burrow}$ was calculated from the lengths of continuous white pixel segments within each horizontal line. The number of burrows N_{burrow} at a specific depth was obtained by dividing the total pixel number in each image line attributed to white structures by the mean burrow diameter $Ø_{burrow}$, expressed in pixel number: $N_{burrow} = \Sigma_{burrowpixels}/Ø_{burrow}$. The number of burrows divided by the area of the sediment–water interface (A_{swi}, expressed in cm^2) gave the burrow density at a specific depth: $\rho_{burrow} = N_{burrow}/A_{swi}$ (number of burrows cm^{-2}). Total burrow length (ΣL_{burrow}) was calculated from the sum of each burrow length (L_{burrow}) in each pixel line, fixed at 0.0083 cm for each horizontal and vertical pixel resolution (cm).

Then, burrow volume at a specific depth (V_{burrow}) was calculated by multiplying the total number of burrows of each pixel line by their specific cylindrical volumes: $V_{burrow} = N_{burrow} \times \Pi \times R^2_{burrow} \times L_{burrow}$ where R_{burrow} = burrow radius = $Ø_{burrow}/2$; L_{burrow} = burrow length fixed at 0.0083 cm for each horizontal and vertical pixel resolution (cm). Here, we report the burrow volume as normalized to the local volume of sediment

$v_{sed} = 0.0083 * A_{swi}$, which then provides $V_{burrow}/V_{sed} = N_{burrow}/A_{swi} \times \Pi \times R^2_{burrow}$ (dimensionless units). If one integrates the local burrow volume V_{burrow} over the whole sediment depth, one obtains the total burrow volume ΣV_{burrow}. The ratio of total burrow volume to the total sediment volume can be expressed as a percentage.

The local burrow wall area (A_{bw}) acts as a proxy of the exchange surface area with overlying water at a given depth and was calculated for each horizontal pixel line by multiplying the number of burrows in each line by the corresponding burrow circumference: $A_{bw} = N_{burrow} \times 2\Pi \times R_{burrow} \times L_{burrow}$. Here, we report the local burrow wall area as normalized to the local volume of sediment: $A_{bw}/V_{sed} = N_{burrow}/A_{swi} \times 2\Pi \times R_{burrow}$ (expressed in cm^{-1}). If one integrates the local burrow wall area A_{bw} over the whole sediment depth, one obtains the total burrow wall area ΣA_{bw}. The ratio of the total burrow wall area ΣA_{bw} over the area of the sediment–water interface represents the exchange surface area extension, which can be expressed as a percentage.

The ratio between depth-integrated burrow wall area and depth-integrated burrow volume A_{bw}/V_{burrow}, gave a single index of the burrow network complexity for the entire aquarium.

d. Sampling and analysis of overlying water

Sediment–water fluxes were measured during closed incubations, in which the flow of water through an aquarium was stopped, while the overlying water in the aquaria remained continuously stirred (~40–60 rpm). Sediment–water fluxes were calculated from the accumulation of solutes in the overlying water, which was followed in two ways: (1) continuous monitoring of the overlying water using planar optical sensors mounted along the inner glass side of each microcosm, and (2) serial sampling of overlying water by removing discrete volumes through the luer locks. Oxygen and TCO_2 fluxes (TCO_2 = total CO_2 = $[CO_2]$+ $[HCO_3^-]$+ $[CO_3^{2-}]$) were measured at two time points: in all 12 aquaria two weeks after initiation of the experiment, between 4 and 15 December (end period 1 = time point 1) and in six aquaria one month after initiation of the experiment between 17 and 24 December (end period 2 = time point 2) (online supplemental file S1). Oxygen and TCO_2 concentrations in overlying water were monitored using planar optodes (time points 1 and 2) and discrete samples (time point 2) every 30 min for a total duration of 2.5 hr, so that oxygen depletion in overlying water was less than 20% below the initial value (Hall et al. 1996). Discrete samples were collected using gas tight syringes. At time point 2, nutrients (NH_4^+, NO_3^-, NO_2^-, TPO_4^{3-} [TPO_4^{3-} = total reactive inorganic P as PO_4^{3-}]) and Br^- (introduced tracer, see below) concentrations were additionally measured in discrete samples.

Approximately one day before the time point 2 sampling, bromide tracer measurements were made to determine solute exchange between overlying water and pore water. In each aquaria, the overlying water, including the reservoir, was replaced with fresh, filtered Long Island Sound seawater (Br^- ~0.7 mM) to which an additional concentration of 5 mM NaBr (sodium bromide) had been added as a tracer (Martin and Banta 1992). This bromide concentration did not significantly affect salinity or solution density.

The oxygen concentration of overlying water was determined by Winkler titration on unfiltered discrete samples. A portion of the remaining water sample was filtered through a 0.2 μm polysulfone inline filter directly into gas tight syringes, and analyzed immediately for TCO_2 using the flow injection method of Hall and Aller (1992) at a precision of 2%–5%. The remaining filtered water was frozen for nutrient analyses. Ammonium was measured using a colorimetric method modified from Solórzano (1969) with a precision 2%–5%. Reactive inorganic phosphate was measured colorimetrically using reduced ammonium molybdate (Presley 1971). Nitrate and nitrite were measured using the Griess reaction in a flow injection analysis mode. Bromide concentrations were determined using a modified phenol red–chloramine T colorimetric method (Presley 1971; Lepore and Barak 2009). All reagents and standards were prepared in acid-washed glassware, and standards were prepared in a nutrient-free artificial seawater matrix. Fluxes were calculated from the slopes of the linear regression of solute concentrations against time in the closed incubations. A correction was made for the composition of the water that replaced each discrete sample (∼50–60 mL) during incubations.

e. Planar optode imaging

Optode membranes (105–126 cm^2 surface areas) for monitoring O_2, pH, and pCO_2 were mounted along the sides of each aquarium, allowing two-dimensional imaging of these parameters to determine benthic fluxes and pore water profiles (online supplemental file S1). O_2 was estimated by direct determination of fluorescence intensity, while pH and pCO_2 concentrations were determined ratiometrically, after initial calibration (Glud et al. 1996; Zhu, Aller, and Fan 2005, 2006a, 2006b).

Optode images were saved in tiff format at a spatial resolution of 45 μm per pixel. Image processing was performed using Matlab (mathworks.com). Because the edges of some optode membranes were damaged, regions of interest (ROI) from the overlying water-to-sediment surface (for benthic fluxes measurements) and from the sediment surface to deeper layers (for pore water concentrations) were selected within the central part of each image. The dimensions of the ROIs were different between each aquarium, but ROIs were taken as large as possible, representing more than 60% of an aquarium side. To avoid any bias, we utilized the entire ROI and did not select specific subareas (e.g., burrows within sediments). For the flux measurements, the same ROI was automatically defined between each picture of the same time series from the same aquarium. In each ROI, intensity values per pixel were transformed into a solute concentration (μM of O_2, pCO_2, and pH) based on calibration of the optode foils. For each pixel, pCO_2 was converted in the corresponding CO_2 (in μM) by using the Henry gas constant $K_0 = 0.034$ mol L^{-1} atm^{-1} at experimental conditions (22°C, 27 S).

To determine TCO_2 accumulation and O_2 consumption, O_2, CO_2, and pH concentrations were first averaged over the entire ROI in the overlying water. Subsequently, TCO_2 was calculated from CO_2 and pH (NBS) using updated forms of the original program CO2SYS

(Lewis and Wallace 1998; Robbins et al. 2010). Dissociation constants of K_1, K_2 (Mehrbach et al. 1973; Dickson and Millero 1987) were used. Flux estimates were then calculated from the slopes of the linear regression of averaged TCO_2 and O_2 values (derived from successive ROIs) against time.

For each ROI within the sediment, the mean, median, standard deviation, and percentiles were calculated for each horizontal line of calibrated pixels. Individual pixel TCO_2 was not calculated because the pH and pCO_2 measurements were made using a different optode and ROI, and thus individual pixel locations differed. The 95th and 5th percentiles indicated the thresholds beyond which the highest and the lowest concentrations are found, respectively. 95th percentiles were calculated for oxygen concentrations and pH, whereas 5th percentiles were calculated for CO_2 concentrations. In this way, extreme values of solute concentrations are considered (lowest, highest), and may represent biogeochemical microenvironments and thus micro-scale heterogeneity.

f. Sampling and analysis of sediment and pore water

i. Remineralization rates To estimate the depth distribution of the organic matter remineralization rate, subsamples of sieved sediment from each depth interval (0–2; 2–4; 4–6; 6–10; 10–15 cm) were incubated anoxically in 50 mL centrifuge tubes (buried in mud) and analyzed serially with time over 43 days to obtain TCO_2 and NH_4^+ net production rates (Aller and Yingst 1980). Pore water was separated by centrifuging subsamples at 3–5 day intervals, filtered through 0.2 μm polysulfone inline filters into gas tight syringes, and analyzed immediately for TCO_2 using the flow injection method of Hall and Aller (1992) at a precision of 2%. Dissolved NH_4^+ was measured colorimetrically using indophenol blue (∼2%–3% precision) (Solórzano 1969). Reversibly adsorbed $NH_4^+$was estimated on subsamples of the centrifuged sediment extracted at 22°C for 1 hr with 2N KCl (Rosenfeld 1979; Mackin and Aller 1984).

ii. Pore water and bulk sediment properties Immediately following the flux incubations, including the Br^- tracer measurements, at time point 2, sediment from six aquaria (CA, CB, SD1, MB, LA, XLA) was sliced into 0.5 cm thick layers from 0 to 2 cm depth, 1 cm layers from 2 to 5 cm depth and 2 cm layers from 5 to 12 cm depth. Subsamples from each interval were taken for porosity, for meiofauna/bacteria measurements (preserved in buffered 2% formaldehyde), and for pH measurements. pH was measured at a precision of 0.1% by direct insertion of a rugged, combination semi-microelectrode after standardization on the NIST (NBS) scale. The remaining sediment was centrifuged (10–15 min, 3,500 rpm) under anoxic conditions. A portion of the pore water was filtered (0.2 μm polysulfone inline filters) into gas tight syringes, and analyzed immediately for TCO_2 (Hall and Aller 1992). Subsamples of the remaining filtered pore water were either frozen for nutrients (NH_4^+, NO_3^-), stored at 4°C for Br^-, or acidified. The subsamples for Fe^{2+}, Mn^{2+}, and TPO_4 analyses were acidified to pH ∼2 with 12N trace metal grade HCl. NO_3^-, NH_4^+, TPO_4 and Br^- were analyzed, as for overlying water. Fe^{2+} and Mn^{2+}were analyzed colorimetrically using Ferrozine and

formaldoxime methods, respectively (Goto, Komatsu, and Furukawa 1962; Stookey 1970). The residual centrifuged sediment was frozen (−20°C) until further analysis of solids. Total carbon (C), nitrogen (N), and sulfur (S) were determined on dried, ground sediment samples using a Carlo Erba (Milan, Italy; carloerbareagents.com) 1102 CHNOS elemental analyzer. Analytical precision, expressed as the relative standard deviation of three replicate analyses, were ±0.8% for N, ±1.6% for C, and ±10.7% for S. Inorganic C was estimated from the quantity of CO_2 released from known weights of dry sediment following acidification with HCl as measured by a micropressure sensor (Schink, Stockwell, and Ellis 1979). The analytical precision for C_{inorg} was ±6% (SD). Sediment porosity was estimated from wet and dry weights of sediment subsamples assuming an individual particle density of 2.5 g cm^{-3}. The sand (>62 μm) and silt-clay (<62 μm) were determined using wet sieving.

g. Bioirrigation modeling

The transport of bromide tracer was simulated using a transient transport model as defined in equation 1, which accounts for both diffusion and nonlocal irrigation (Emerson, Jahnke, and Heggie 1984). The model assumes a constant porosity with depth and time, a fixed volume of overlying water, a constant core area, and time-independent transport coefficients during the tracer incubation period.

$$\begin{aligned} \frac{\partial C}{\partial t} &= D_s \frac{\partial^2 C}{\partial z^2} + \eta(C_T - C) \qquad (1)\\ t = 0; \quad & C = C_0, 0 \le z \le L \\ t > 0; \quad & C = C_T(t), z = 0 \\ & \frac{\partial C}{\partial z} = 0, z = L \\ & \eta = f(z), 0 \le z \le L_B \end{aligned}$$

where

$C(z, t) = Br^-$ concentration in pore water (C_0 = constant)
t = time after injection of the tracer
z = depth; coordinate origin at interface, positive into sediment
D_s = diffusion coefficient, constant
$\eta(z)$ = nonlocal transport coefficient, function of depth
$C_T(t)$ = time-dependent solute concentration in overlying water of fixed volume, V.
L = depth of sediment (impermeable base of aquarium)
L_B = depth of bioirrigated zone (nonlocal transport zone; $L_B \le L$)

The model equations were solved numerically using a forward, fully explicit approach using a centered finite difference scheme (checked for accuracy by analytical solutions for specific cases). The nonlocal transport coefficient was assumed to either decrease exponentially below a specific depth (e.g., $\eta = \eta_0 e^{-\alpha_0 z}$; η_0, α_0 constants; for $z < L_B$; or below L_B)

or to remain entirely constant over a depth interval ($\eta = \eta_0$ for $z < L_B$). The latter approximation with $L_B = 4$–6 cm was found suitable to fit Br^- profiles over the relatively short incubation time of 18–24 hr. An additional nonlocal term that attenuated with depth below L_B was necessary for modeling TCO_2 and NH_4^+ distributions as outlined subsequently. To properly connect the two zones ($z < L_B$ and $L_B < z < L$), the continuity of fluxes and concentrations were assumed at $z = L_B$. The value of η was taken as 0 in controls.

h. data processing

The sediment column was reorganized into four main sediment layers according to Berger's model (Berger, Ekdale, and Bryant 1979), as a function of classical distributions of biogenic structures in coastal sediments (Gerino 1992): 0–2 cm (mixed layer), 2–4 cm (sub-mixed layer), 4–6 cm (mixed layer transition), >6 cm (not-mixed layer). Solute concentrations derived from 2-D optodes were averaged for each horizontal pixel line. Concentration values and burrow parameters from each pixel line were used as pseudo-replicates of the appropriate sediment layer (0–2 cm; 2–4 cm; 4–6 cm; > 6 cm) for each aquarium (XL, L, M, S, C). Statistical differences in burrow geometry parameters and 2-D solute concentrations were tested between depth layers (0–2 cm; 2–4 cm; 4–6 cm; >6 cm), size classes (aquaria XL, L, M, S), and their interactions (aquaria × layer) with PERMANOVA analysis with 999 permutations and $\alpha = 0.05$ (Anderson 2017). To determine which burrow geometry parameters (V_{burrow}/V_{sed}, L_{burrow}/V_{sed}, A_{bw}/V_{sed}, A_{bw}/V_{burrow}) and biogeochemical fluxes (TCO_2, O_2, NO_3^-, Br^-) explained the most variability among *Nephtys* treatments, a principal component analysis (PCA) was performed on the correlation matrix. Data were normalized prior to analysis. Finally, correlation analyses were used to quantify the relatedness between variables with the non-parametric Spearman multicorrelation analysis for the entire sampling period, after data normality verification. The correlation coefficients of Spearman ρ quantifies the statistical dependency between variables (i.e., the strength of the correlation). All statistical analyses were conducted within the R environment (R Development Core Team 2021) and relied on the vegan (Oksanen et al. 2020) and FactoMineR (Lê, Josse, and Husson 2008) packages.

3. Results

a. Bulk sediment properties

Porosity in the two control aquaria averaged 0.844 ± 0.008 in the surface layers (0–1 cm) and decreased slowly to 0.778 ± 0.001 at depth (~8 cm). Porosity in the treatments with animals was slightly higher at the surface (0.871 ± 0.003) but decreased to similar values at depth (0.775 ± 0.007 at ~8 cm). The depth-averaged porosity across all aquaria was 0.78 ± 0.06. Wet sieving revealed an average sand content of 2.60 ± 1.37% weight (median 2.65%), and a 97.4 ± 1.37% silt-clay content. There was no significant difference in particle size between depth intervals. The organic C (C_{org}), total N, and total sulfur contents of the sediment ranged 2.24%–2.36%, 0.25%–0.26%, and 0.68%–0.72%,

Table 2. Characteristics of the depth-integrated burrow geometries from X-radiography for the four size classes over time from the initial day (+15 days, +22 days, +26 days): total sediment volume (V_{sed}, cm^3), total area of the sediment–water interface (A_{swi}, cm^2), burrow radius (R_{burrow}, cm), burrow length (L_{burrow}, cm), burrow volume (V_{burrow}, cm^3), and burrow wall area (A_{bw}, cm^2), V_{burrow}/V_{sed} ratio (%), A_{bw}/A_{swi} ratio (%), and A_{bw}/V_{burrow} ($.cm^{-1}$).

Size class	Time of analysis	V_{sed} (cm^3)	A_{swi} (cm^2)	R_{burrow} (cm)	L_{burrow} (cm)	V_{burrow} (cm^3)	A_{bw} (cm^2)	V_{burrow}/V_{sed} (%)	A_{bw}/A_{swi} (%)	A_{bw}/V_{burrow} ($.cm^{-1}$)
XL	15 d	521	41	0.20	26	3.26	32	0.63	78.1	9.82
	22 d	590	47	0.20	52	6.60	65	1.12	138	9.85
	26 d	479	39	0.20	45	5.70	57	1.19	146	10.0
L	15 d	536	43	0.15	54	3.80	51	0.71	119	13.4
	22 d	479	39	0.15	63	4.50	60	0.94	154	13.3
	26 d	492	40	0.15	78	5.50	73	1.12	183	13.3
M	15 d	550	44	0.10	106	3.30	66	0.60	150	20.0
	26 d	485	39	0.10	159	5.00	100	1.03	256	20.0
S	15 d	520	42	0.05	165	1.30	52	0.25	124	40.0
	22 d	484	39	0.05	147	1.10	46	0.23	118	41.8

respectively, with no obvious differences with depth or between aquaria (online supplemental file S2). The inorganic C content (C_{inorg}), assumed to be entirely $CaCO_3$, was 0.23 ± 0.03% at the start of the incubation (n = 5; all depths) and averaged 0.20 ± 0.08% across all aquaria at the termination of the experiment (online supplemental file S2). The mean value of C_{org} = 2.31 ± 0.27%, mean C_{org}/N_{total} = 10.5 ± 1.7 (mol/mol), and mean total sulfur = 0.69 ± 0.20% (online supplemental file S2).

b. Burrow structures

The visible images from the side of aquaria and the binarized images from X-radiography (Fig. 1) showed clear differences in *Nephtys* burrowing networks between size treatments (XL, L, M, S) 15 and 26 days after the beginning of the experiment. After fauna addition, the smallest individuals burrowed sooner than the adult ones. Total burrow length was largest for juvenile worms; burrow structures for juveniles stabilized as soon as the beginning of the experiment (Table 2).

At the time of sediment sampling (+26 days), burrow diameters were generally smaller than the measured width of individuals, and burrow radii ranged from 0.05 cm for S to 0.2 cm for XL individuals (Table 2). The burrows of largest animals (XL) had fewer branches than those of the smaller animals, which had numerous interconnected extensions (Fig. 1). The burrow density (ρ_{burrow}; Fig. 2a) ranged between 0.01 and 0.7 burrows cm^{-2} at the surface, and significantly increased in subsurface layers (0–2 cm depth; 0.2; 0.4; 1; 1.4 burrows cm^{-2} for XL, L, M and S aquaria, respectively). The ρ_{burrow} is particularly high at the surface and subsurface layers for the M and S treatments. ρ_{burrow} was significantly lower for the larger size classes ($p < 0.001$; XL < L < M < S) up to 6 cm depth, and became significantly higher down to 6 cm depth for the XL aquarium ($p < 0.001$) where the other size classes

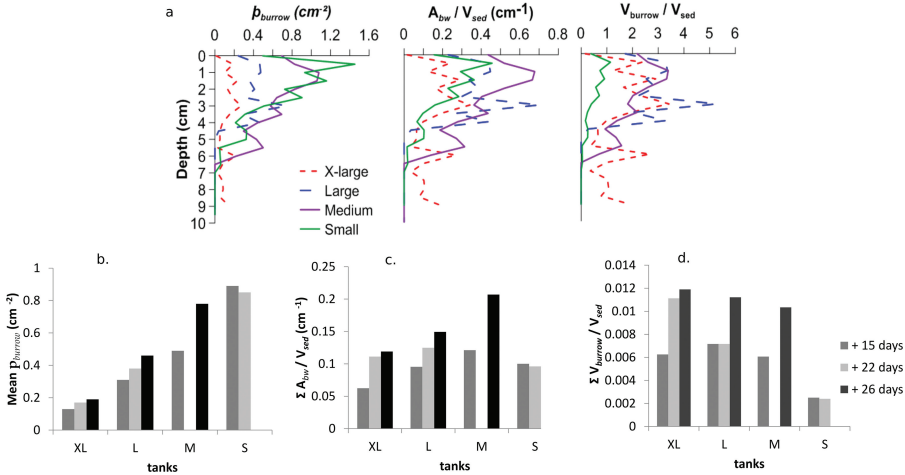

Figure 2. *Nephtys incisa* burrowing activity. The upper panel (a) shows the depth-dependant data averaged every 0.5 cm up to 10 cm depth for all the inhabited aquaria (18–24 December 2007): burrow density ρ_{burrow}, burrow wall area A_{bw}/V_{sed}, and burrow volume (V_{burrow}/V_{sed}) normalized to the sediment volume. The lower three panels (b, c, d) show the corresponding depth-integrated data: (b) mean burrow density over first 4 cm (cm^{-2}); (c) total burrow wall area (A_{bw}/V_{sed}; cm^{-1}); (d) total burrow volume (V_{burrow}/V_{sed}) at 15, 22, and 26 days after the start of the experiment.

were absent. ρ_{burrow} were similar at 2–4 cm depth between M and S aquaria ($p > 0.23$), and at 4–6 cm depth between XL and L aquaria ($p > 0.42$) (Fig. 2a). Averaged over the first 4 cm depth, the burrow density was highest with the smallest individuals during all the duration of the experiment (Fig. 2b).

Normalized burrow wall areas ranged between 0.1 and 0.5 cm^{-1} over the first 4 cm, and increased in the following order XL < S < L = M (Fig. 2a). Beneath 4 cm, A_{bw}/V_{sed} significantly decreased with depth for each aquarium ($p < 0.001$), but the M and XL treatments retained a high A_{bw}/V_{sed} between 4 cm and 6 cm depth and beneath 6 cm, respectively ($p < 0.01$). At the final time point, and when integrated over the whole sediment volume, the surface extension due to burrow walls was highest for the M treatment (250%), followed by L (182%), XL (146%), and S (119%) (Table 2 and Fig. 2c).

Burrow volumes did not follow the same depth trend as the burrow wall areas. In the surface layer, V_{burrow}/V_{sed} ranged between 0.5% and 3% in the order S < XL < M <L ($p < 0.01$). In subsurface layers (2–4 cm), XL and L treatments had the largest burrow volumes (more than 3%; $p < 0.01$). While the XL aquarium had the highest V_{burrow}/V_{sed}, down to 10 cm ($p < 0.01$), the M still had important V_{burrow}/V_{sed} at 6 cm depth compared with the L treatment ($p < 0.01$). Integrated over the whole sediment volume, ΣV_{burrow} were the highest for the largest size classes in the following order XL > L > M, and six times bigger than the S size class ($p < 0.01$) (Fig. 2d). Consequently, A_{bw}/V_{burrow} ratios were twice and four times larger for the smallest size S relative to the XL and L sizes, respectively.

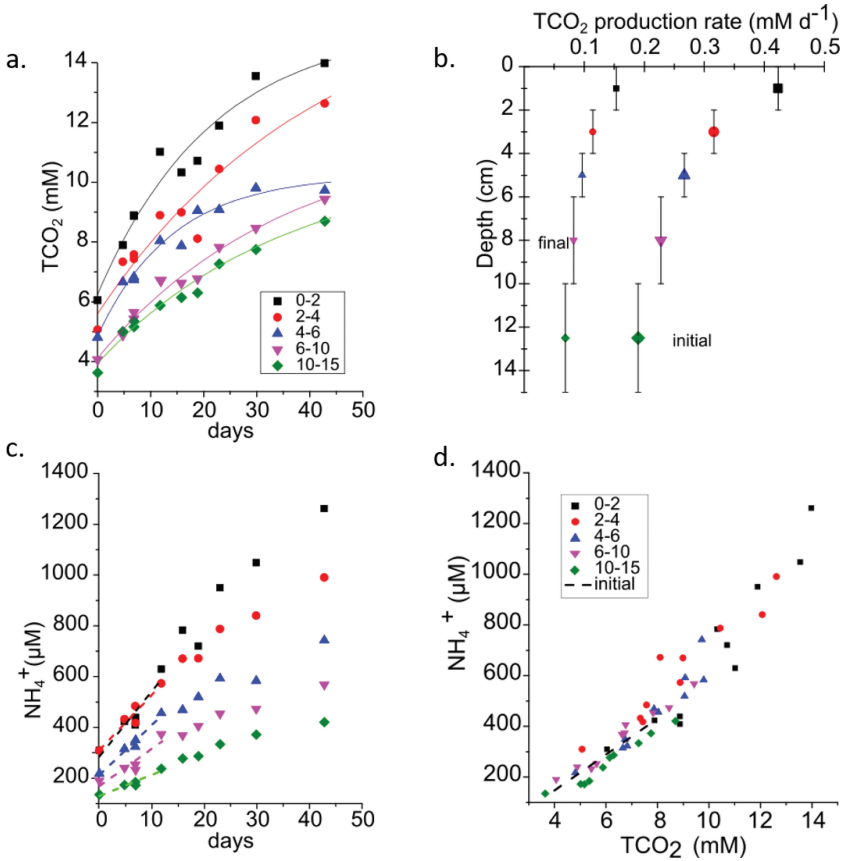

Figure 3. TCO_2 and NH_4^+ functions of time and depth. (a) TCO_2 production rate as a function of time in anoxic incubations of sediment from the different depth intervals in experimental aquaria (0–2, 2–4, 4–6, 6–10, 10–15 cm). The polynomial curves represent the fits used to derive TCO_2 production rates as a function of time. (b) TCO_2 production rates (mM d^{-1}) as a function of depth at the beginning and end of the experimental period. (c) NH_4^+ as a function of time in anoxic incubations from the same depth intervals. The dashed lines represent fits used to estimate initial production rates of NH_4^+ after correction for adsorption. (d) NH_4^+ against TCO_2 in anoxic incubations. The initial stoichometric relationship (12 d) is shown by the dashed line (geometric mean N/C slope = 74.2 mmol/mol; adsorption corrected C/N slope = 4.1; assuming $K = 2.25$).

c. Sediment remineralization rates

The TCO_2 in anoxically incubated sediment samples increased linearly with time over the first ~12 days (constant accumulation rate), with a progressive decrease in the accumulation rate thereafter (Fig. 3a). The TCO_2 evolution in each depth interval over 43 days was fit by an exponential function of the form $C = C_1(1 - e^{(-kt)}) + C_0$, where $C_0, C_1, k =$ constants, consistent with a single fraction of reactive organic matter with a first order

decomposition rate constant k (Westrich and Berner 1984). The asymptotic stabilization suggests a relatively small quantity of reactive organic matter that is gradually exhausted (see online supplemental file S3). Because TCO_2 increased with incubation time, these patterns may also partially reflect precipitation of carbonate in closed anoxic incubations. This could be particularly relevant in the surface-most layers, where TCO_2 increases were greatest, and thus remineralization rates may be underestimated. If sustained for 30 days, the highest rate (0.42 mM d^{-1}, initial rate in the first 2 cm; Fig. 3b; see also online supplemental file S3) would have resulted in a decrease in solid C_{org} of ~0.02% wt., assuming a porosity of ~0.8, which is at the limit of detection of an elemental analyzer. We refer to the pool of organic material that supports the rapid production of TCO_2 (and NH_4^+) during these anoxic incubations as "reactive" organic matter. A decreased production of TCO_2 supported by less reactive organic matter pools was expected over longer time periods (Westrich and Berner 1988; Burdige 2006). Assuming a uniform average reaction constant $k = 0.039 \pm 0.020$ d^{-1} (n = 5; see online supplemental file S3), the observed TCO_2 production rate has the form of the curve fits: $R = (R_0 e^{-\alpha z} + R_1) e^{-kt}$; where R_0, R_1 are remineralization rates (mM d^{-1}), z = depth below sediment–water interface (cm), α = depth attenuation constant (cm^{-1}) (Fig. 3b). The depth integrated production supported by the initial rates ($t = 0$; $z = 15$ cm) was 30.4 mmol m^{-2} d^{-1} (adopting the average porosity = 0.78; $R_1 - 0.309$; $R_0 = 0.184$ mM d^{-1}; $\alpha = 0.267$ cm^{-1}). This would correspond to the expected TCO_2 flux from the sediment at steady state, if the reactive C_{org} pool was not depleted and assuming no effect of biogenic transport activities on remineralization (Fig. 3b). Assuming time-dependent decrease in C_{org} remineralization rates, the approximate minimum expected supported TCO_2 flux is ~9.4 mmol m^{-2} d^{-1} at 30 days (depth integration of the remineralization function, $R(z, t)$, at $t = 30$ d).

The NH_4^+ accumulation patterns with time were similar to those for TCO_2 (Fig. 3c). Time-dependent increases of NH_4^+ in each depth interval were fitted by a similar exponential function: $C = C_1(1 - e^{(-kNt)}) + C_0$, (where C_0, C_1, k_N = constants) (see online supplemental file S4). Estimates of k_N were smaller than for TCO_2 ($k_N \sim 0.024 \pm 0.005$ d^{-1}). A decrease in remineralization rate with time is consistent with a relatively small pool of reactive organic matter, and $k_N < k_C$ implies carbonate precipitation affected TCO_2 accumulation in incubations. During the first 12 days, a linear increase of NH_4^+ characterized the pore water (online supplemental file S4). The average reversible adsorption coefficient of NH_4^+ was $K = 2.25 \pm 0.66$ (SE slope; adopting an average porosity of 0.78). After correction for reversible adsorption (multiplier factor $[1 + K]$) and porosity, we estimated a depth-integrated NH_4^+ production rate of 6.1 mmol m^{-2} d^{-1} (over the first 12 days), which is the expected sediment–water flux of NH_4^+ at steady state in all aquaria assuming no additional reactions (e.g., no nitrification, denitrification) or decay of substrate with time. The molar C/N remineralization ratio (depth integrated TCO_2 production rate divided by NH_4^+ production rate) was therefore ~5.0, which is slightly larger than the adsorption corrected regression slope of TCO_2 against NH_4 pore water concentrations in the incubations over the first 12 days (Fig. 3d).

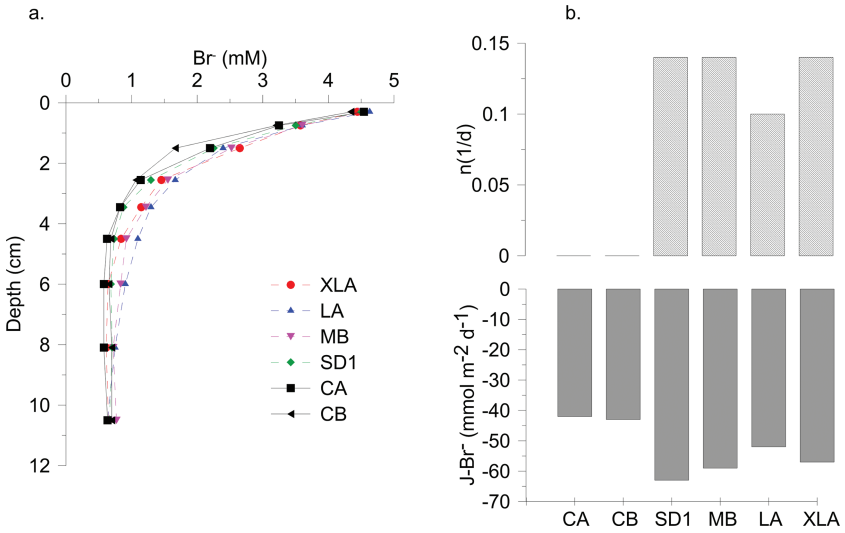

Figure 4. Bromide (Br^-) tracer. (a) Br^- penetration patterns in aquarium sediment. (b) Br^- fluxes (J-Br^-, mmol Br^- m^{-2} d^{-1}) and nonlocal transport coefficient (d^{-1}) calculated from Br^- pore water profiles in the controls and *Nephtys* size class aquaria.

d. Pore water solute distributions

i. 1-D non-reactive solute distributions and transport: Bromide. Bromide penetrated into the microcosm sediments over the 18- to 24-hour exposure period. The aquaria containing *Nephtys* showed a deeper penetration depth of the bromide signal, and a higher bromide inventory (concentration integrated over depth) relative to controls (Fig. 4a). We assumed the controls showed only diffusion and not nonlocal bioirrigation, and the resulting sediment diffusion coefficient (D_s) for Br^- in the controls was 1.12 ± 0.1 cm^2 d^{-1}. For different tortuosity relations, and adopting a porosity of 0.78, temperature of 22 and salinity of 27, the theoretically expected D_s is in the range 1.00–1.08, depending on the exact tortuosity model (Boudreau 1997). This same D_s value was used when fitting the Br^- depth profiles of the *Nephtys* aquaria. The modeled nonlocal transport coefficients for Br^- were $\eta_0 =$ 0.14, 0.10, 0.14, and 0.14 d^{-1}; $\alpha_0 = 0$ (all cases); and $L_B = 4.5$, 6, 5, and 4 cm in the XL, L, M, and S aquaria, respectively (Fig. 4b). The measurements of the overlying water Br^- concentrations were compromised analytically, and so fluxes could not be calculated from the Br^- decrease in the overlying water. Model predicted fluxes of Br^- into the sediment (based on pore water depth profile fitting) were 42 and 43 mmol m^{-2} d^{-1} for CA and CB, and 63, 59, 52, and 57 mmol m^{-2} d^{-1} for SD, M, L, and XL, respectively, at the time of Br^- sampling, and represent approximate flux enhancements of $\sim 1.4 \pm 0.1$ in all *Nephtys* aquaria (Fig. 4b).

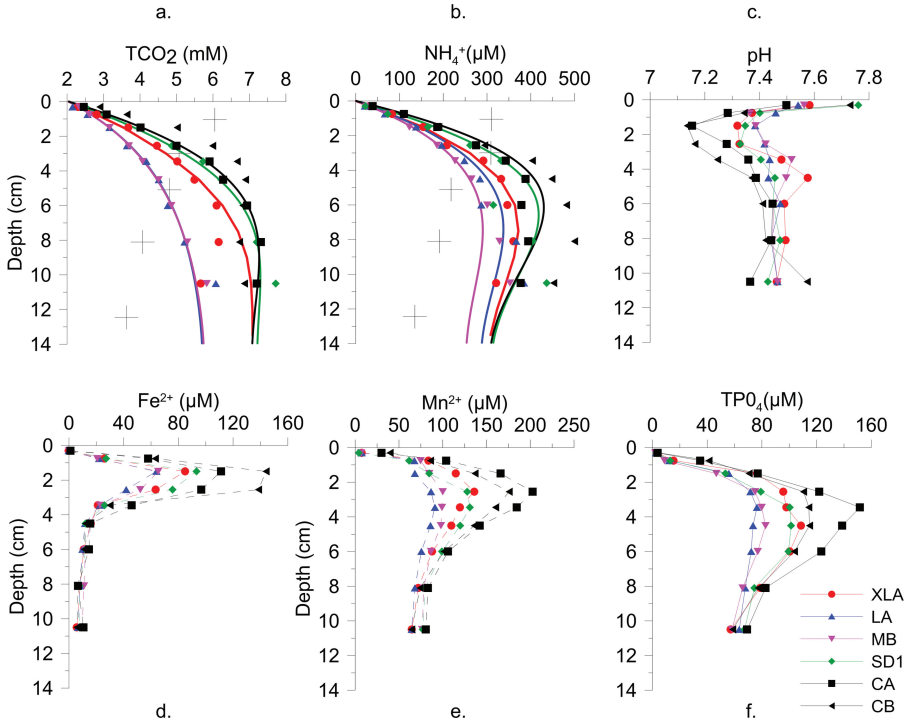

Figure 5. Vertical pore water profiles. (a) TCO_2 and (b) NH_4^+ pore water profiles at $t = 0$ (solid vertical bars) and after ~4 weeks in the experimental aquaria (symbol plotted at midpoint of sample depth interval). Transient nonlocal transport–reaction model profile fits are shown as solid lines for CA, S, M, L, and XL tanks. There was a Δ_t relative to initial profiles for CA (26 d), S (27 d), M (27 d), L (29 d), XL (27 d), and CB (32 d). 1-D profiles of reactive solutes distribution at the end of the experiment: (c) pH, (d) Fe^{2+}, (e) Mn^{2+}, (f) TPO_4. The dashed curves are plotted to aid viewing of distributions.

ii. 1-D reactive solute distributions: TCO_2 and NH_4^+, pH, TPO_4, Fe^{2+}, and Mn^{2+}. The pore water distributions of TCO_2 and NH_4^+ within aquaria differed substantially one from another at the times of sampling, with the highest accumulation observed in controls and lower concentrations in the aquaria containing *Nephtys* (concentrations in M $\leq$ L $<$ XL $<$ S $<$ CA $<$ CB; Fig. 5a and b). The TCO_2 and NH_4^+ profiles were modeled using a transport–reaction model consistent with the Br^- nonlocal transport rates obtained for each aquarium and the estimated time–depth dependent production rates of TCO_2 and NH_4^+ based on $R(z, t)$ at the time of sampling (Fig. 3). The model equations for each solute (i) are given in the online supplemental file S5, and the model parameters used for the XL, L, M, and S aquaria are presented in supplemental file S6. To obtain good fits to the upper 8–10 cm of the profiles of TCO_2 and NH_4^+ in *Nephtys* aquaria, while using the reaction rates as measured in the anoxic incubations, we found it was necessary to assume that nonlocal transport

extended deeper than indicated by Br^-. In these cases, the nonlocal transport functions were assumed to be constant over the depth interval defined by Br^- penetration (i.e., L_B), but below L_B, nonlocal transport was apparently not zero. In the absence of additional tracer data, it was assumed that below L_B, nonlocal transport attenuated exponentially with depth (Martin and Banta 1992). The depth attenuation constants (α_0) of nonlocal transport below depth L_B necessary to obtain fits to the upper 8–10 cm of the profiles were comparable for both TCO_2 and NH_4^+ (see online supplemental file S6). Thus, the profiles of both TCO_2 and NH_4^+, were consistently fit by assuming the transport parameters obtained from Br^- tracer analysis ($\eta = \eta_0$; $\alpha_0 = 0$; $L < L_B$), an additional nonlocal transport term at depth ($\eta = \eta_0 \exp(-\alpha_0 z)$, $L \geq L_B$), and the remineralization rates derived from the anoxic incubation series. Although distributions within the intensely burrowed zone were reasonably fit by the model for TCO_2 and NH_4^+, the NH_4^+ concentrations within deepest depth intervals remained underestimated, indicating that reaction rates could be underestimated in the deeper intervals (up to ~0.5 μM d^{-1} below ~8 cm), possibly due to the use of a single k_C ($= -0.039\ d^{-1}$) for the time dependence of all reaction rates (online supplemental file S6).

The vertical profiles of pore water pH, Fe^{2+}, Mn^{2+}, and TPO_4 (total dissolved inorganic P) (Fig. 5c–f) were typical in their overall depth dependence to those commonly observed in organic-rich, marine muds. There were clear subsurface minima (pH) or maxima (TPO_4, Fe^{2+}, and Mn^{2+}) present 1–4 cm below the upper oxidized sediment surface. Maxima (peak concentrations of TPO_4, Fe^{2+}, and Mn^{2+}) and minima (pH) were more pronounced in controls compared to aquaria with *Nephtys*, and the relative deviations in concentrations (maxima) from control profiles were in approximately the same order as observed for TCO_2 and NH_4^+ concentrations: L ≤ M < XL < S < CB < CA.

iii. 2-D distributions of reactive solutes: O_2, CO_2, pH. For each 2-D optode image, the background (0.01–0.1 μM O_2) was below detection and could not be distinguished from zero with this methodology. Oxygen concentrations decreased rapidly below the sediment surface for all aquaria, and highest averaged concentrations (~200 μM O_2) were found only in the first millimeters below the sediment surface (Fig. 6). Mean and median oxygen values remained significantly higher in the upper 0–2 cm of inhabited sediments compared with the control aquarium ($p < 0.001$), and the controls showed a conspicuous subsurface minimum in O_2. The presence of the larger animals slightly enhanced oxygen in subsurface and deeper layers, with highest subsurface concentrations for the L aquarium (2 μM O_2; $p < 0.001$) followed by the XL and M aquaria. While volume-averaged O_2 concentrations remained very low, images showed oxidized sediment in and around burrows in each inhabited aquarium (Fig. 6a and b). 2-D oxygen concentrations were uniformly low sharply below the sediment surface in the control aquarium and otherwise at analytical background (undetectable), whereas O_2 distributions were more heterogeneous with animals (Fig. 6a). The highest oxygen concentrations in deep layers are obscured by the mean and median calculations (Fig. 6c), but they are revealed by larger standard deviations over depth in the

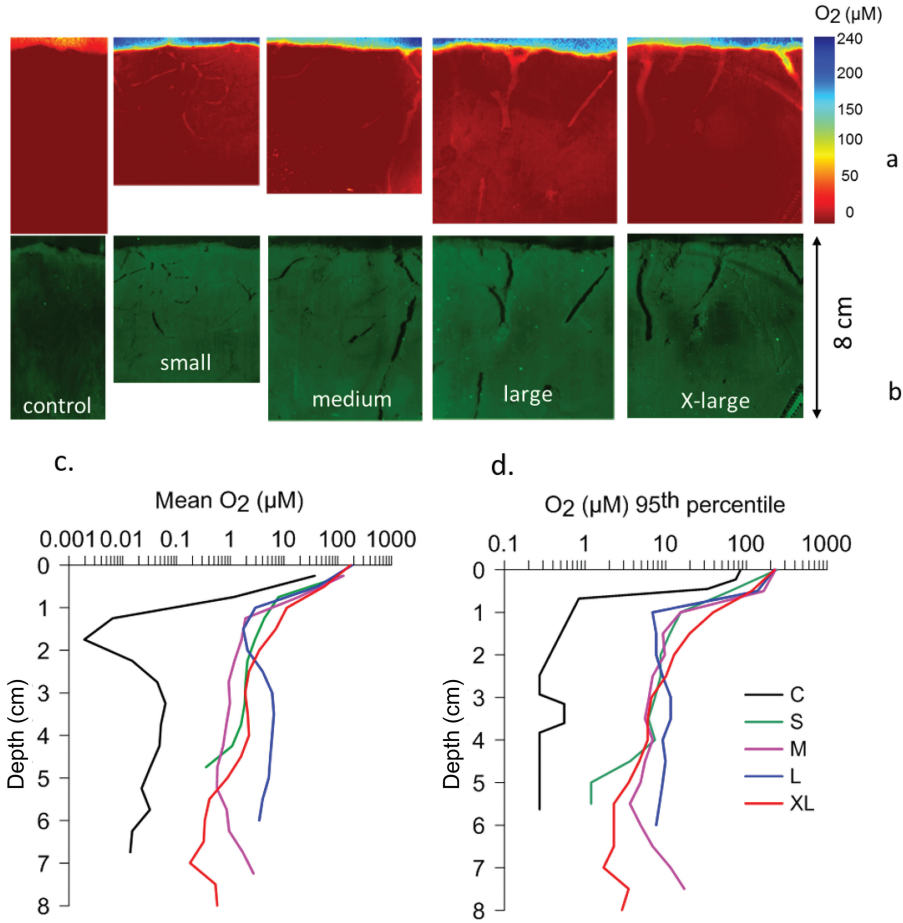

Figure 6. *Nephtys incisa* burrows and O_2 concentrations (18–24 December 2007). (a) Pictures from sides of the aquaria showing the fluorescence results of the O_2 fluorosensor in all treatments and (b) visible views. (c) O_2 concentrations. (c) Oxygen 95th percentiles averaged every 0.5 cm to 10 cm depth for the XL, L, M, S, and C treatments.

Nephtys inhabited sediments than in control aquaria (e.g., 95th percentiles; Fig. 6d). The burrows visible in pictures were often oxygenated and surrounded by a relatively O_2 rich zone (Fig. 6a and b). These oxidized microenvironments were associated with the highest subsurface O_2 concentrations with order L > XL > M > S > C (Fig. 6d).

2-D CO_2 distributions showed different patterns (Fig. 7). Horizontally averaged CO_2 concentrations increased rapidly below the sediment surface with the large animals (100 μM CO_2; $p < 0.001$). Below 2 cm, the control aquarium reached maximum concentrations (200 μM CO_2; $p < 0.001$). CO_2 concentrations were significantly lowered in layers

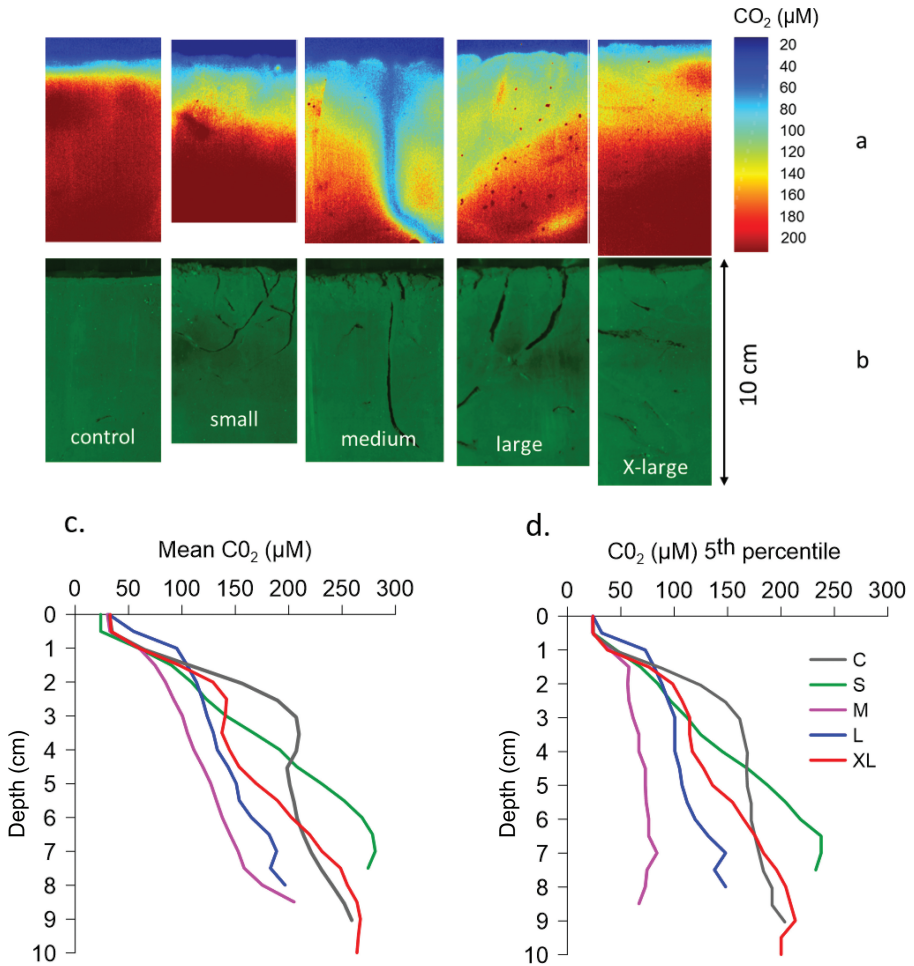

Figure 7. *Nephtys incisa* burrows and O_2 concentrations (18–24 December 2007). (a) Pictures from sides of the aquaria showing the radiometric fluorescence results of the CO_2 fluorosensor in all treatments and (b) visible views. (c) CO_2 concentrations. (d) CO_2 5th percentiles averaged every 0.5 cm to 10 cm depth for the XL, L, M, S, and C treatments.

impacted by large burrows down to 8 cm depth in the order M < L < XL < S (100–250 µM, respectively; $p < 0.001$; Fig. 7c). The median in each pixel line was similar to the averaged concentration. Standard deviations around the means in the control were low and homogeneous with depth, whereas they were more variable in the order S < XL < L < M aquaria. Burrows affected the CO_2 concentrations vertically. Low averaged CO_2 concentrations (100–150 µM) were measured in deep layers where burrows were observed (Fig. 7a and b), the most distinctive example of which was the M aquarium. A CO_2 concentration

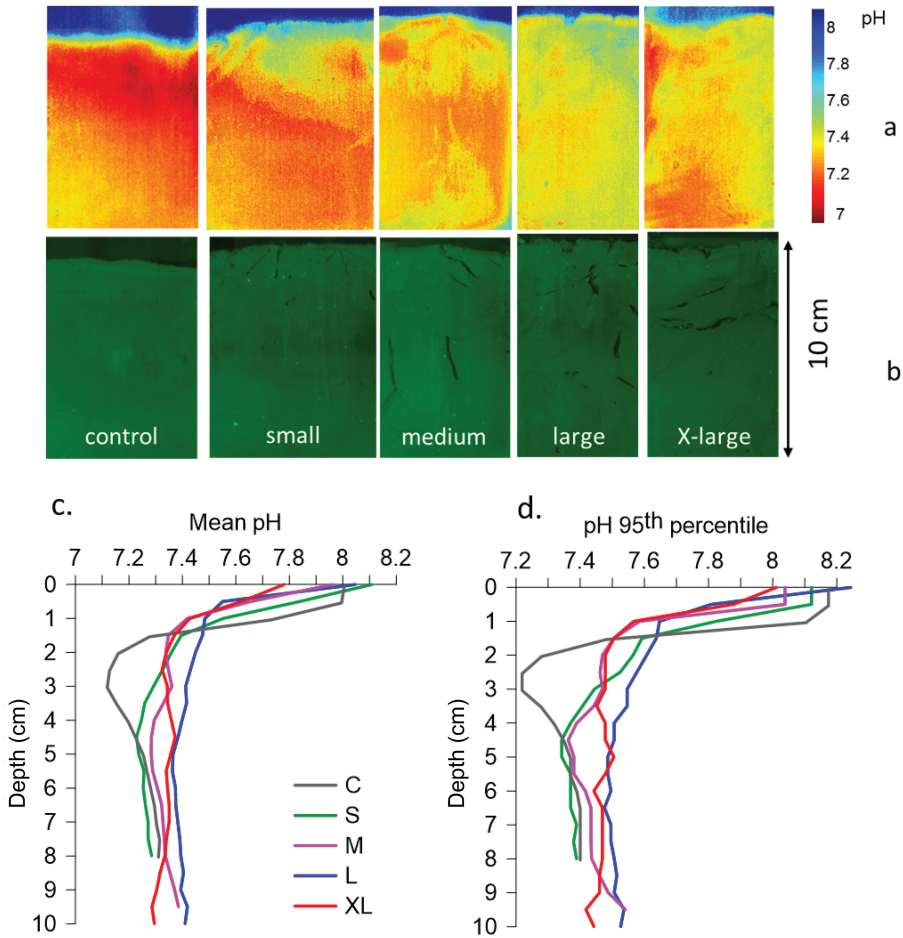

Figure 8. *Nephtys incisa* burrows and pH (18–22 December 2007). (a) Pictures from sides of the aquaria showing the radiometric fluorescence results of the pH fluorosensor in all treatments and (b) visible views. (c) pH. (d) pH 95th percentiles averaged every 0.5 cm to 10 cm depth for the XL, L, M, S, and C treatments.

gradient is observed around each burrow in the optode images (Fig. 7a and b). The lowest CO_2 concentrations are associated with the presence of burrows and oxidized microenvironments around them for M and L aquaria (50–100 μM) from 1 cm deep (Fig. 7d).

2-D pH distributions showed an overall decrease of average pH with depth below the sediment–water interface, with a distinct subsurface minimum in the control aquarium (mean pH ~7.1–7.2) between 1–4 cm (Fig. 8a and c). Additionally, the pH in the upper ~1 cm remained nearly constant in the control aquarium (Fig. 8c), while it decreased below the sediment surface in the aquaria with worms. Low attenuation or constant pH within the

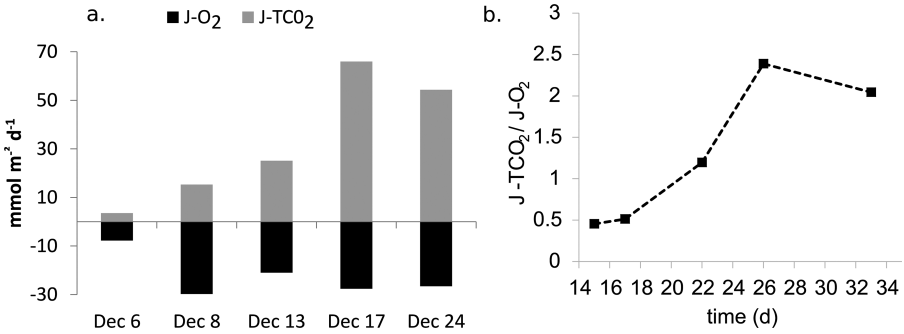

Figure 9. Oxygen uptake (J-O_2, mmol O2 m^{-2} d^{-1}) and total CO2 release (J-TCO_2, mmol TCO_2 m^{-2} d^{-1}). (a) Measured in the control aquaria over all the duration of the experiment (6, 8, 12, 17, and 24 December 2007; ranging 15–33 d after experiment initiation) from the planar optodes. (b) TCO_2/O_2 flux ratios against time for the control aquaria.

upper 0.5–1 cm of the S and M aquaria was also occasionally seen (95th percentile) (Fig. 8d). pH values increased in surface and subsurface sediments inside and around burrows. The highest pH values (95th percentile) was measured for XL > S > L = M (Fig. 8d) between 2 cm and 4 cm depth. The distinct subsurface minimum of pH evident in the control largely disappeared in aquaria inhabited by worms ($p < 0.001$; Fig. 8c). Minima of pH were heterogeneously distributed (7.2–7.4) with depth around the burrows (see M aquarium in Fig. 8a and b). Horizontally averaged pH (mean pH) of 7.4 to 7.6 at depth (below 4 cm) were significantly higher in the presence of XL and L animals, respectively ($p < 0.001$; Fig. 8a and b), classes for which the 95th percentiles have the highest pH (Fig. 8d).

e. Net solute fluxes: TCO_2, O_2, NO_3^-

Because we analyzed the solute fluxes via discrete sampling in the four control aquaria on five different dates (6, 8, 13, 17, 24 December; ranging 15–33 d after experiment initiation; see online supplemental file S1), we have a proxy of the time evolution of the experimental system without macrofauna (Fig. 9). The measured O_2 flux (J-O_2) into sediment quickly increased from −7.7 to −30 mmol O_2 m^{-2} d^{-1} (within the first 15 d) and remained nearly constant afterward. TCO_2 flux (J-TCO_2) increased progressively to higher rates over time (3.5–65 mmol TCO_2 m^{-2} d^{-1}) (Fig. 9a). A plot of J-TCO_2/J-O_2 against time demonstrates that the net flux ratio was initially < 1, increased to ∼1.4 by three weeks, and thereafter continued to increase rapidly to ∼2–2.2 (Fig. 9b).

Planar optodes fluxes for O_2 and TCO_2 were derived at two time points, after 15 days (period 1) and 30 days (period 2) (Fig. 10; supplemental file S1). Initially (period 1), fluxes increased from control treatments to higher values progressively with animal size (XL > L > M > S > C) according to logarithmic relationships (J-O_2 = 23.62ln(x) – 62.58; $R^2 = 0.87$ and J-TCO_2 = −92.61ln(x) + 169.17; $R^2 = 0.98$; Fig. 10a and b). The same pattern was

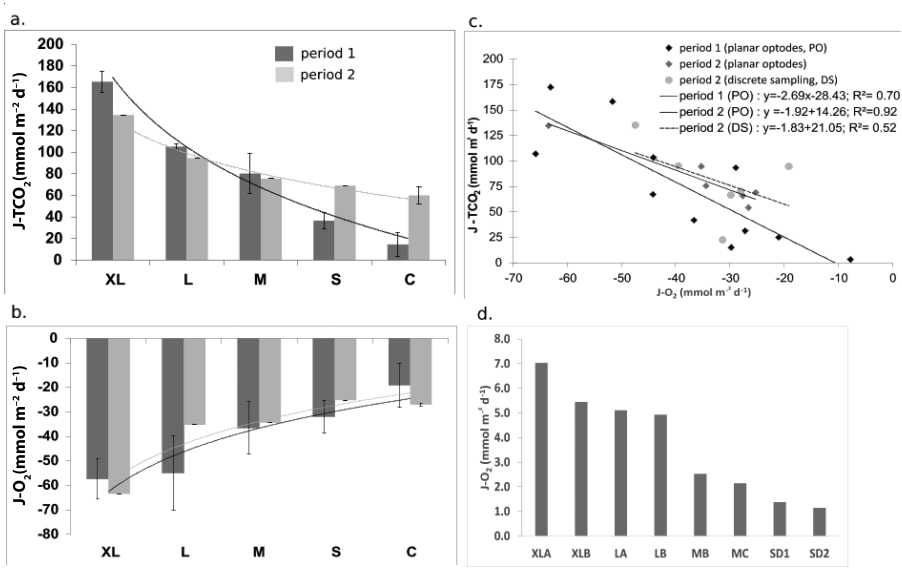

Figure 10. Total CO_2 fluxes (J-TCO_2, mmol TCO_2 m^{-2} d^{-1}) and oxygen uptake (J-O_2, mmol O_2 m^{-2} d^{-1}). (a) Total CO_2 fluxes and (b) O_2 uptake measured in all the aquaria (C, S, M, L, XL) with planar optodes, at the end of period 1 (averaged fluxes, n = 2 for the inhabited aquaria, n = 4 for the control aquaria) and at the end of period 2 (single fluxes for each inhabited aquarium and averaged fluxes for the control aquaria, n = 2). The logarithmic relationships and equations between fluxes and size structure are in the main text. (c) Linear correlations between J-O_2 and J-TCO_2 at the two periods of the measurements, with the different ways to measure the fluxes (planar optodes and discrete sampling). (d) Macrofauna respiration O_2 fluxes (mmol O_2 m^{-2} d^{-1}) for all the aquaria; the values were corrected to 22C using a Q_{10} of 2.5 (Shumway 1979).

seen at the second time point with regression coefficients (J-O_2 $= 22.74\ln(x) - 58.86$; $R^2 = 0.88$ and J-TCO_2 $= -46.08\ln(x) + 131.01$; $R^2 = 0.98$; Fig. 10a and b), but without replication of the individual treatments. Comparisons between the two methods (planar optodes and discrete sampling) for measuring oxygen uptake and TCO_2 effluxes showed good overall agreement (online supplemental file S7). Oxygen uptake ranged from ~ -7 to -63 mmol O_2 m^{-2} d^{-1} and TCO_2 release from 3 to 172 mmol TCO_2 m^{-2} d^{-1}, reaching magnitudes that greatly exceeded the steady state flux predicted from the anoxic remineralization rates.

There is good relationship between O_2 and TCO_2 fluxes during period 1 of the experiment ($R^2 = 0.70$, $p < 0.05$), with a geometric mean slope of the correlation: $\Delta TCO_2/\Delta O_2 = -2.69$ (Fig. 10c). The flux ratios using optical and discrete samples at the end of period 2 ranged from -1.92 ($R^2 = 0.92$) to -1.83 ($R^2 = 0.52$) (Fig. 10c; $p < 0.05$). During both period 1 and 2, the ratios of fluxes were greater than predicted from steady state stoichiometric models of aerobic respiration of organic matter only ($\Delta TCO_2/\Delta O_2$ ~0.75

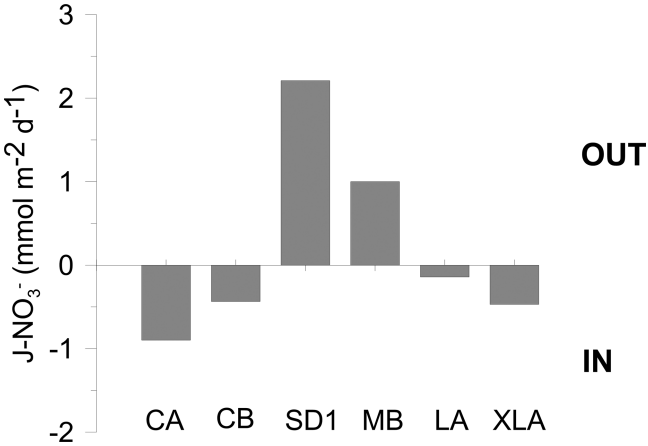

Figure 11. Nitrate fluxes (J-NO_3^-, mmol NO_3^- m^{-2} d^{-1}) measured in the overlying water by discrete sampling of each treatment at the second period.

assuming complete nitrification). We compared the TCO_2, CO_2, alkalinity concentrations, and the resulting benthic fluxes from the various analytical methods used and found excellent agreement (i.e., flow injection, pH electrode) (online supplemental file S8).

Nitrate fluxes (period 2) were distinguished by effluxes from sediment into the overlying water in the S and M treatments with values ranging 1–2.2 mmol NO_3^- m^{-2} d^{-1}, and by influxes into the sediments in the Control, L, and XL treatments with values of -0.1 to -0.9 mmol NO_3^- m^{-2} d^{-1}, respectively (Fig. 11). Phosphate fluxes were below detection in all cases and thus not shown.

f. Relationships between burrow structures and benthic fluxes

The PCA analysis explained 90% of the variability among the aquaria and various sampling dates over the whole duration of the experiment. The first axis explained 53.8% and the second axis 36.9% (Fig. 12). The most important variables (and their loadings) defining the first axis were the L_{burrow}/V_{sed} (0.98), A_{bw}/V_{sed} (0.90), A_{bw}/V_{burrow} (0.87) and bromide fluxes (-0.96), while the V_{burrow}/V_{sed} (0.68), NO_3^- fluxes (0.84), O_2 fluxes (0.83) and TCO_2 fluxes (-0.86) defined the second axis. Aquaria were separated into five groups on the basis of PCA results. Sampling dates for each aquarium group are clustered. Sampling dates for each group of aquaria had little effect on aquarium groupings. The S and M treatments were characterized by the PCA as having high NO_3^- released into overlying waters and the higher total lengths of burrows and denser burrows networks (A_{bw}/V_{burrow}). The volumes of burrows coupled to the TCO_2 effluxes group the replicates of L and XL treatments, whereas the burrow wall areas group M and L treatments.

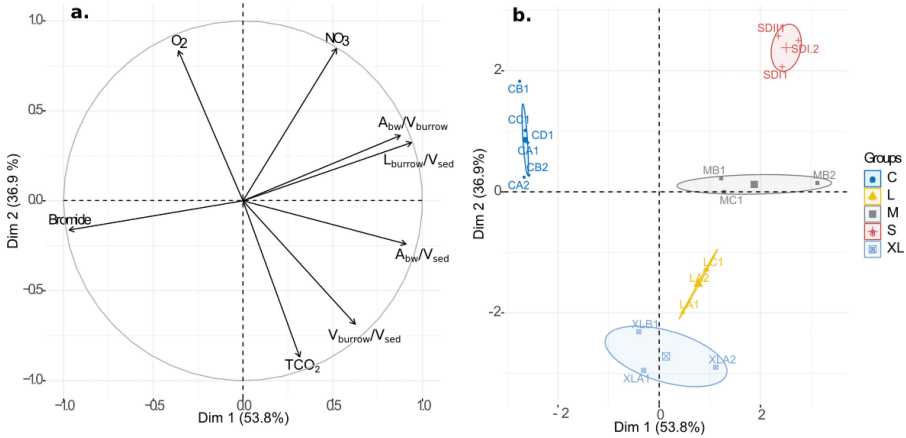

Figure 12. Principal component analysis based on the burrow geometry ($V_{\text{burrow}}/V_{\text{sed}}$, $L_{\text{burrow}}/V_{\text{sed}}$, $A_{\text{bw}}/V_{\text{sed}}$, $A_{\text{bw}}/V_{\text{burrow}}$) and biogeochemical fluxes (TCO_2, O_2, NO_3^-, Br^-) measured in the replicates of control and in the replicates inhabited aquaria over the duration of the experiment (involving two periods of measurements). The two axes pictured explain 90.7% of the variability in the treatments data. Dim: dimension.

The correlation matrix in the online supplemental file S9 indicated significant relationships between the biogeochemical variables and the burrow geometries based on the Spearman correlation coefficients ($p < 0.05$). The geometry variables of burrows were significantly intercorrelated (A_{bw}/V_{burrow} and $L_{burrow}/V_{\text{sed}}$). Oxygen uptake and nitrate fluxes were negatively associated to TCO_2 effluxes with an increasing burrow length and $A_{\text{bw}}/V_{\text{burrow}}$ ratios (Fig. 13). The TCO_2 and nitrate fluxes were correlated with the burrow volumes (online supplemental file S9).

4. Discussion

The primary purpose of this study was to evaluate whether a single species of infauna (the polychaete *Nephtys incisa*) can influence sediment biogeochemistry and solute fluxes differently depending on the age–size stage. To provide a common basis for comparison, biovolume (∼biomass) was fixed across all four size classes and abundances were adjusted.

a. Burrowing patterns of the Nephtys incisa populations

Infaunal burrowing patterns can reflect the depth-dependent availability of reactive organic matter in deposits and variation in physical properties, such as porosity (Michaud, Aller, and Stora 2010). With some exceptions (Norling et al. 2007), most experimental studies of bioturbation have homogenized sediment over depth intervals that are large relative to natural compositional gradients (>10 cm). To minimize artifacts in the burrowing responses of the different *Nephtys* size classes, we retained the natural reactive substrate

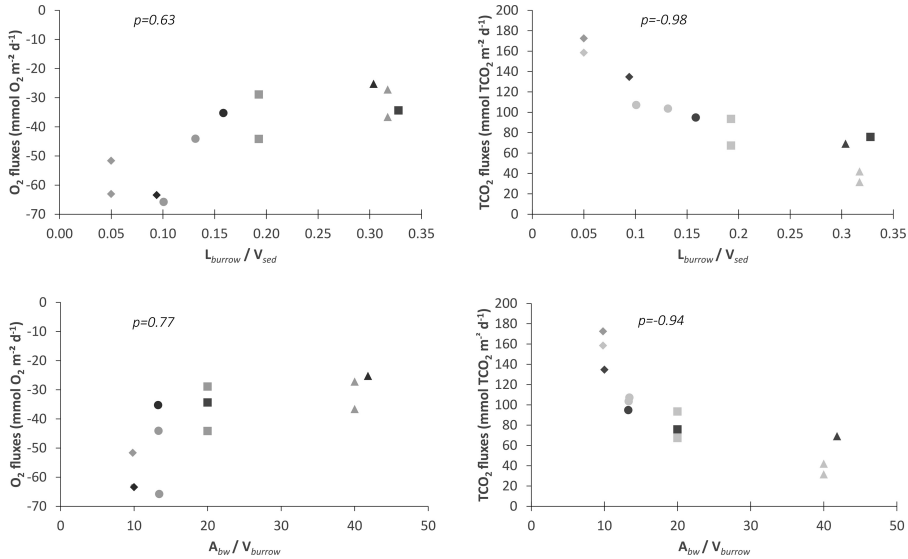

Figure 13. O_2 and TCO_2 fluxes at the sediment–water interface as a function of the burrows geometry variables ($L_{\text{burrow}}/V_{\text{sed}}$, $A_{\text{bw}}/V_{\text{burrow}}$) in all the inhabited aquaria for the two periods of the experiment. (a) O2. (b) TCO_2. Period 1 (gray); period 2 (black). Spearman correlations (ρ) are indicated on each graph. The various shapes distinguish the aquaria: diamonds (XL), circles (L), squares (M), and triangles (S).

and porosity distributions as much as possible. Both the magnitudes and the depth attenuations of TCO_2 and NH_4^+ production rates (Fig. 3b) in the aquaria were comparable to those found previously in central Long Island Sound (attenuations: 0.3–0.8 cm^{-1}; Aller and Yingst 1980; Westrich and Berner 1988). We therefore assume that the observed burrowing patterns reflect typical behavior in natural deposits that have exponential decreases of reactive organic matter and porosity with depth. Miron et al. (1991) found that shape and length of nereid burrows are density dependent, burrows being smaller and more "I-" or "L-" rather than "U"- shaped at high densities of adults. In our case, natural densities and typical biovolumes were used for individual size classes, and we think that alteration of burrow geometries due to spatial overlap of structures was also minimized.

The $A_{\text{bw}}/V_{\text{burrow}}$ ratio was higher for the smallest size classes (Table 2), showing that burrows of juveniles are more complex than those of adults. The burrows of juvenile worms (S, M) are 6–7 times longer in aggregate than XL and L burrows, but are distributed over a shallower sediment depth (0–4 cm), making them denser in the subsurface. In contrast, the burrows of adult worms (L and XL) are deeper (to 10 cm depth) but are less dense and complex. This suggests that a *Nepthys* individual does not make its burrow more complex (no supplementary burrow branch) during growth (passage from juveniles to adult stage) but makes it larger relative to its own biovolume. Total burrow volumes were thus highest for the

larger size classes. When the burrows grow, the burrow wall areas remain similar between S and XL size classes, and the burrow volume increases only for XL. It is at the intermediate age stage (M, L) that the burrow wall areas are the most important. Calculations from the burrow geometries thus reveal that the network density of burrows and burrow heterogeneity depend on the body size classes and are not proportionally linked to the total biovolumes of worms. For the same total biovolume and within the same volume of sediment, the bigger burrow volumes over depth were generated by the largest size classes, while the burrow wall areas were increased in the order M = L > S = XL up to 4 cm depth, with a higher burrow complexity in the order S > M > L > XL. The different burrowing depths of animals depend on their size, but also likely on their musculature and on the geotechnical properties of sediments. For the juvenile *Nephtys*, whose metabolism is less demanding and proboscis (for foraging) less developed (Trevor 1978), it is likely much easier to burrow where mud is less compacted ($\Phi > 0.88$) (Trevor 1976; Dorgan 2015; Crane and Merz 2017).

b. Non-reactive solute transport

At the time of final sampling, the lowest sediment–water Br^- flux was in the control ($\sim$40 mmol $m^{-2}d^{-1}$) and resulted largely from physically controlled diffusion. Br^- fluxes in the aquaria inhabited by *Nephtys* ($\sim$60 mmol m^{-2} d^{-1}) resulted from both physical diffusion and biological nonlocal transport. The factor of $\sim$1.4 increased flux of Br^- into bioturbated deposits demonstrates that burrow structures were at least periodically ventilated, and that radial exchange between sediment and burrow water took place around them. Despite the substantial differences in burrow geometry distributions between the *Nephtys* size classes and different burrowing exchange areas, however, the internal transport regimes as measured by Br^- nonlocal transport coefficients (0.1–0.14 d^{-1}), were very similar in the presence of *Nephtys*, and approximately independent of size class and burrow density.

This tendency can be understood by considering the relationship between nonlocal transport coefficients and burrow diffusion geometries. The burrow spacing and diameters are relatively constant over depth intervals of 4–6 cm, and up to as much as $\sim$9 cm for the XL size class (Fig. 2). Using the cylinder microenvironment model (Aller 1980), we can approximate solute diffusion geometry and scaling in this upper burrowed zone, which dominates Br^- transport in each aquarium, as a set of evenly spaced hollow cylinders of length L_B separated on average by a distance $2r_2$ and having burrow radii r_1 determined by respective burrow width (e.g., Table 2). Boudreau (1984) showed that at steady state, an approximate relationship between the cylinder model geometry and the nonlocal exchange coefficient is given by

$$\eta \approx \frac{D_s r_1}{(r_2^2 - r_1^2)(\bar{r} - r_1)} \tag{2}$$

where $\bar{r}$ = radial position at depth z where the radially averaged solute concentration occurs.

This relationship, (equation 2), assumes a linear concentration gradient of solute from r_1, the inner burrow wall surface, to $\bar{r}$. The nonlocal approximation to the cylinder model

also holds for unsteady conditions, at least for unreactive solutes, and a given value of η can correspond to any of an infinite set of geometric combinations (Aller and Yingst 1985; Aller 1988). If the linear gradient in $C(r)$ is assumed to extend to r_2, and if $r_1 << r_2$, then equation 2 simplifies further to

$$\eta \sim \frac{D_s r_1}{(r_2^2 - r_1^2)(\frac{2}{3} r_2 - r_1)}. \quad (3)$$

From equation 3, the measured values of η (0.14; 0.1, 0.14, 0.14 d^{-1}; Fig. 4) and r_1 (0.05, 0.1, 0.15, 0.2 cm; Table 2) imply approximate values for r_2 of 0.87, 1.2, 1.3, and 1.45 cm (S, M, L, XL). So the mutual increase of both r_2 (lower burrow density) and r_1 (larger size burrow) result in a nearly constant η. The measured spacing of burrows in X-radiographs indicates an expected range of r_2 of 0.25–0.5 (S, M); 0.75 (L), and 1.5 (XL). This spacing allows conversion of the burrow network into cylindrical burrow equivalents with estimated r_2 of 1.3, 1.9, 2.7, and 3.8 cm (S, M, L, XL), or into bifurcated burrows with estimated r_2 of 0.95, 1.3, 1.9, and 2.7 cm. Remarkably, these various measured and modeled estimates are in a comparable range and in the relative order of magnitude, particularly given uncertainties regarding exactly how burrows are ventilated (e.g., which sections and how frequently). Most important, however, these calculations demonstrate that it is reasonable that the different sets of geometrical dimensions of the burrow structures could produce similar averaged transport conditions for a *non-reactive* tracer such as Br^- despite substantial variation in faunal density and individual size.

c. Reactive solute distributions

i. TCO_2 and NH_4^+ average transport–reaction relationships. The pore water distributions of TCO_2 and NH_4^+ can be generally well simulated by combining the nonlocal transport parameters derived from Br^- analysis and the production rates independently derived from the anoxic incubation time series (Figs. 3–5). The primary exceptions are that additional nonlocal transport had to be included below a depth L_B, and that the NH_4^+ production rates appear to be underestimated, or transport is overestimated, at depth (below 8 cm). Underestimation of NH_4^+ production at the time of sampling is likely due to an overestimate of reactive organic matter decay rate for both C and N ($k_C \sim 0.039$ d^{-1}). Because of the relatively coarse sampling resolution of the averaged pore water profiles, the transport–reaction model fits are not particularly sensitive to departures from the estimated reaction rates, positive or negative, in the upper ~1 cm or in microenvironments surrounding burrows. The effects of any loss of NH_4^+ due to nitrification in the surface region or around burrows, for example, were undetectable in the depth interval averaged pore water profiles.

Cable bacteria (Meysman 2018) were found to be present in surface sediment of all aquaria, with the longest filaments in the control aquarium CA (microscopic observation J. Aller, pers. comm.). Unfortunately, because sediment samples were stored for years before cable filament cell enumeration, counts were not considered sufficiently accurate

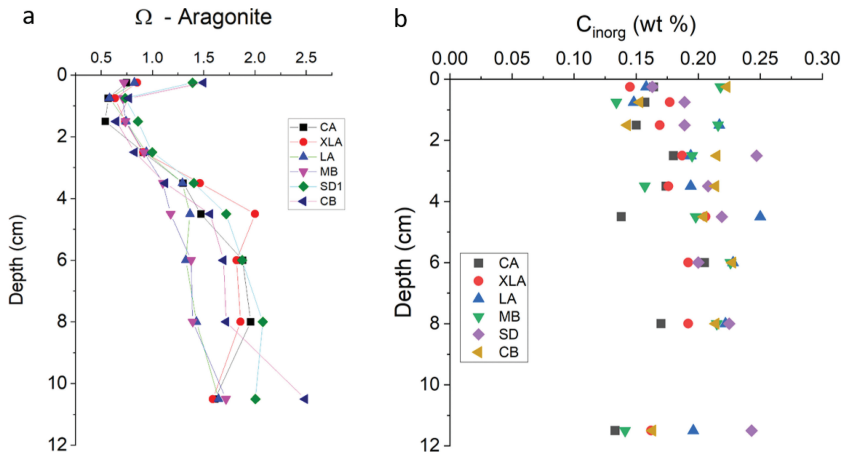

Figure 14. Aragonite and inorganic C saturation states. (a) Aragonite (Ω) in bulk pore water samples as a function of depth in the experimental treatments at the end of period 2. (b) Inorganic C ($\sim CaCO_3$) in sediment as a function of depth in sampled aquaria at the end of period 2. The depth-averaged value in sediment (0–15 cm) was $0.23 \pm 0.03\%$.

to report numerically. The pH profiles in the CA control at the end of period 2, indicate that cable bacteria were likely active, with comparatively limited attenuation of pH in the upper ~1 cm and a distinct subsurface minimum at 2.5–3 cm (Meysman et al. 2015). Although near interface pH gradients were also minimized in a small percentage of optical profiles obtained from the M and S aquaria (Fig. 8d), suggestive of localized cable bacteria activity, the average pH profiles in the aquaria with worms indicate that cable bacteria activity did not dominate average patterns. Their activities may have potentially altered reaction mechanisms and balances, particularly around burrows (Aller et al. 2019), but the general agreement between the modeled pore water distributions of ΣCO_2 and NH_4^+ in surface sediment with the independently measured transport rates (Br^-) and reaction rates estimated from anoxic incubations suggests that, if active, they did not alter organic matter mineralization to an extent detectable with the sampling resolution. There was also no evidence of net accumulation of authigenic carbonates in the oxic surface zone (Nielsen and Risgaard-Petersen 2015), and in fact a net loss of C_{inorg} from surface sediment was observed in all aquaria (Fig. 14). As discussed subsequently, cable bacteria likely affected sediment–water fluxes of TCO_2 and O_2–TCO_2 relationships in the control aquaria after an initial ~3-week period.

The difference in modeled nonlocal transport functions between Br^- and TCO_2 and NH_4^+ (attenuation with depth) may be explained in part by differences in the relative time scales associated with the solute distributions and by burrow irrigation patterns, or by differences in net reaction rates. Br^- penetrations reflect transport and responses over a relatively short period (18–24 hr), whereas the TCO_2 and NH_4^+ distributions represent transport–reaction conditions averaged over a more extended period (up to ~26–32 d). The handling of aquaria

during experimental manipulations may also induce burrow irrigation and activity behavior that differs from the averaged longer term patterns, for example, the temporary retreat of individuals into deeper regions of burrows than they might normally be positioned. With respect to mineralization rates, it is possible that NH_4^+ production is slightly enhanced underneath the relatively intensely irrigated surface zone or in proximity to burrows relative to closed anoxic incubations because of the decrease in inhibitory metabolites (Aller 1978, 1988); however, the control aquaria showed similar behavior to that in the biologically irrigated aquaria, implying that the NH_4^+ remineralization rate is underestimated at depth by the serial anoxic incubations in all cases (Fig. 3).

ii. pH, TPO_4, Fe^{2+}, Mn^{2+} distributions and biogenic transport–reaction structure. The transport–reaction structure generated by *Nephtys* substantially affected the average distributions of H^+, TPO_4, Fe^{2+}, and Mn^{2+} relative to controls (Fig. 5). As noted previously, in the control aquaria, these properties were likely strongly influenced by cable bacteria in the upper few centimeters during time period 2 and at the time of final sampling (Nielsen and Risgaard-Petersen 2015; Meysman 2018). Intense burrowing is known to inhibit cable bacteria activity (Malkin et al. 2014; Yin et al. 2021), so that one effect of *Nephtys* is to create conditions that minimize the influence of cable bacteria on spatially averaged sediment properties and fluxes such as those measured in this study. Thus, comparison of the control distributions and those associated with *Nephtys* likely represents a contrast between conditions dominated by macrofauna–bacteria consortia and those dominated by cable bacteria activity. The pore water distributions demonstrate that peak concentrations of Fe^{2+}, Mn^{2+}, and TPO_4 (averaged over $\sim$189 cm^2) can vary by $\sim$30 to $\sim$100 μM between *Nephtys* aquaria at the burrow densities present and also are distinctly lower than in controls. Unfortunately, for highly reactive solutes the complex transport–reaction patterns formed by *Nephtys* cannot be accurately simulated by the same nonlocal transport models derived from Br^- (Aller 2001; Meile et al. 2005). These models assume horizontal homogeneity of pore water concentrations and transport fluxes in direct proportion to $\eta(z)$ and the mean burrow water–pore water differences at any given depth (Boudreau 1984, 1997). The supply of oxidants (O_2, NO_3^-) along burrow walls usually creates oxic–suboxic microenvironments and significant local sinks for dissolved Fe^{2+}, Mn^{2+}, and TPO_4 that may be stable or highly transient (Meile et al. 2005). We interpret the differences in the Fe^{2+}, Mn^{2+}, and TPO_4 distributions between aquaria as reflecting these processes, consistent with enhanced burrow wall exchange areas and oxidized microenvironments in the presence of *Nephtys* (Fig. 15). Future studies should better resolve reactive solute distributions such as Fe^{2+} at the microenvironment scale.

d. Net fluxes of reactive solutes TCO_2, O_2, and NO_3^-

Relative to control aquaria, the presence of *Nephtys* clearly altered the net fluxes of TCO_2, O_2, and NO_3^-, and did so in patterns associated with worm sizes (Figs. 10, 11, and 13). The

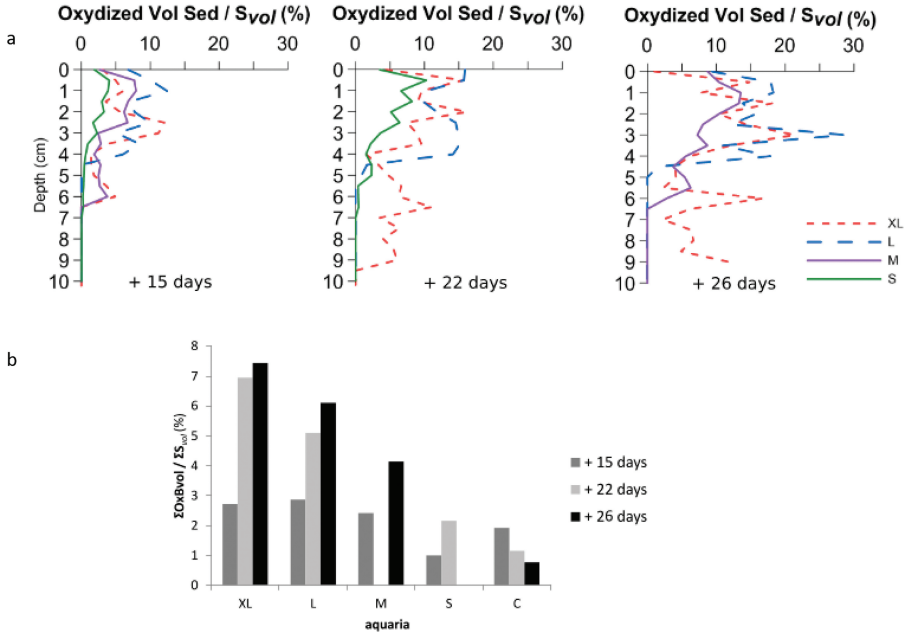

Figure 15. Oxidized sediment volume. (a) As a function of depth and time in experimental inhabited aquaria. (b) The column graph represents the depth-averaged values for each sampling period for the inhabited (XL, L, M, S) and control (C) aquaria.

fluxes of both TCO_2 and O_2 increased as worm sizes increased. Part of this pattern reflects direct O_2 consumption and respiration by *Nephtys*. Assuming that the general O_2 uptake pattern of errant polychaetes applies to *Nephtys*, then: O_2 uptake (10°C) = 0.344($B^{0.61}$) mL O_2 h^{-1} g dry wt^{-1} (B = biomass – g dry wt; Shumway 1979). Converting the wet biomass values of *Nephtys* in each aquarium by assuming a dry/wet ratio of 0.15 and assuming $Q_{10} = 2.5$ to correct O_2 consumption from 10 to 22°C, we estimated that *Nephtys* contributed an average of 6.24, 5.02, 2.33, and 1.26 mmol O_2 m^{-2} d^{-1} to the sediment water O_2 flux for XL, L, M, and S aquaria, respectively (Fig. 10d). An equivalent flux of TCO_2 would result if a respiratory quotient of one were assumed for *Nephtys*. The sediment was sieved through a 1 mm mesh and therefore contained meiofauna that affect both transport and reaction rates at the sediment–water interface and stimulate oxic processes in the bioturbated zone (Aller and Aller 1992; Piot, Nozais, and Archambault 2014); however, we cannot accurately evaluate this possible contribution, and we assume it is much less than the direct impact of macrofaunal biomass in these experiments.

After subtracting these estimated *Nephtys* respiratory contributions from the average total measured fluxes of O_2 and TCO_2 for period 1, the residual fluxes are: J-O_2 = −51.1, −49.9, −34.2, −30.6, and −19.1 mmol m^{-2} d^{-1}; and J-TCO_2 = 159,

100, 78.0, 35.5, and 14.6 mmol m^{-2} d^{-1} for XL, L, M, S, and C, respectively. The ratios of J-O_2 in *Nephtys* aquaria to the control flux average = 2.7, 2.6, 1.8, and 1.6, implying substantial additional sinks for O_2 that correlate directly with worm size. The additional sinks may reflect stimulation of remineralization rates, increased dissolved and solid phase metabolite reoxidation (e.g., NH_4^+, Mn^{2+}, Fe^{2+}, FeS_2) by macrofauna, and unsteady conditions enhanced by burrowing.

Similarly, the J-TCO_2, corrected for direct macrofaunal contributions, clearly exceeds the magnitudes expected from sedimentary aerobic respiration alone at steady state. Assuming that a portion of the O_2 flux is consumed by nitrification only, then further subtracting 0.77 * J-O_2 from J-TCO_2 results in residual J-TCO_2 (period 1) of 120, 61.8, 51.7, 11.9, and −0.1 mmol m^{-2} d^{-1} for XL, L, M, S, and C aquaria, respectively. This excess J-TCO_2 may reflect unsteady fluxes during active burrowing, contributions from anaerobic metabolism including coupled nitrification–denitrification and SO_4 reduction, and carbonate dissolution. We expect that any unsteady fluxes from initial inventories of pore water TCO_2 would decline with time. If all of the initial pore water TCO_2 above seawater background were flushed from an aquarium sediment, approximately 283 mmol m^{-2} would have been available. If all the initial pore water TCO_2 were released uniformly over a 14- to 28-day period, excess J-TCO_2 fluxes of 20 to 10 mmol m^{-2} d^{-1} could have resulted, respectively. We think that it more likely that most initial pore water TCO_2 was released to overlying water during the first few days of the experiment when worms began to burrow. In either case (pulsed or uniform release rate), the initial conditions are unlikely to dominate the TCO_2 fluxes at the times they were measured.

The ratios of O_2 and TCO_2 fluxes are suggestive of a major role of $CaCO_3$ dissolution in all treatments and *Nephtys* aquaria in particular. If we assign all acid production from aerobic oxidation of organic matter (including nitrification) with Redfield ratios of C/N/P (106/16/1) to the dissolution of $CaCO_3$, then a J-TCO_2 / J-O_2 of 1.67 would be expected if reactions go to completion (Emerson, Grundmanis, and Graham 1982). If there is no contribution from nitrification or if coupled nitrification–denitrification occurs, the flux ratios can be 1.78 (coupled nitrification–denitrification) to 2 (no nitrification, no TPO_4 release). The measured total flux ratios (1.8–2.7; Fig. 10c) are consistent with substantial $CaCO_3$ dissolution but also with additional processes not tied directly to O_2. In the absence of Ca^{2+} and Mg^{2+} analyses, we cannot be sure of the exact balance between the contributions of multiple possible reactions, including anaerobic remineralization, but we conclude that much of the excess TCO_2 relative to O_2 must reflect $CaCO_3$ dissolution and coupled nitrification–denitrification, and that these net reactions are enhanced differentially by *Nephtys* size classes in the order XL > L > M > S. Although it is known that bioturbation activities can increase $CaCO_3$ dissolution and associated alkalinity fluxes from both muds and sands (Green, Aller, and Aller 1992; Rao et al. 2014), the present results reveal the complexity of the interactions of these reactions with community structure.

A further evaluation of the likely role of $CaCO_3$ dissolution in elevating J-TCO_2 comes from mineral saturation states. The average pore water in all aquaria was distinctly

undersaturated with respect to aragonite and calcite in the upper ~3 cm, consistent with substantial $CaCO_3$ dissolution and elevated J-TCO_2 (Fig. 14). As noted earlier, we believe that during period 2, cable bacteria were active in the control aquaria, which likely explains supersaturation of $CaCO_3$ in the upper 0–1 cm at the termination of the experiment, but not in *Nephtys* inhabited aquaria (Fig. 14). Largely undetectable bulk solid phase changes are expected given the range of observed J-TCO_2 and the variability in measured values of inorganic C (~$CaCO_3$) (Fig. 14b). If for example, $CaCO_3$ supported a TCO_2 flux of 50 mmol m^{-2} d^{-1} from the upper 6 cm (typical primary bioirrigation depth based on Br^-) for 30 days, then an average loss of ~48 μmol g^{-1} would be required (porosity = 0.79; bulk density ~0.53 g cm^{-3}). This loss corresponds to ~0.05% C_{inorg}, which is not detectable in bulk samples given measurement variability (Fig. 14b).

If $CaCO_3$ dissolution was largely focused into oxidized microenvironments associated with burrows or the uppermost surface layer, loss should have been analytically detectable in burrow walls. Unfortunately, we did not separately dissect and measure burrow wall compositions. O_2 is heterogeneously distributed over sediment depth as dictated by the complexity of burrow networks, and this heterogeneity cannot be revealed by simple averaged concentrations (Wenzhöfer and Glud 2004; Pischedda et al. 2008, 2012). The likely role of redox microenvironments in producing the net flux patterns is supported circumstantially by examination of the total oxidized sediment volume and production rates in the different aquaria (Fig. 15). Both the volume magnitude and production rates of oxidized sediment during burrow formation vary directly in the order XL > L > M > S > C, in the same relative sequence as the enhancement of J-O_2 and J-TCO_2. Dornhoffer, Waldbusser, and Meile (2012) illustrated by modeling how biogeochemical heterogeneity caused by burrows can affect oxygen distribution inside sediment and total oxygen uptake. In our study, microenvironments along *Nephtys* burrow walls likely promoted aerobic C_{org} remineralization and the reoxidation of metabolites such as Fe sulfides (e.g., pyrite, FeS_2), Fe^{2+}, Mn^{2+}, enhancing the dissolution of $CaCO_3$ disseminated through the deposit as well as the escape of anaerobically generated HCO_3^-.

As in the case of O_2 and TCO_2, and in sharp contrast to nonreactive Br^-, there were strong density and size dependent effects of *Nephtys* on the net NO_3^- fluxes across the sediment–water interface (Fig. 11). The highest NO_3^- flux observed was ~2.2 mmol m^{-2} d^{-1} for the S aquaria, corresponding to ~40% of the expected total remineralized N flux (~5.4 mmol m^{-2} d^{-1}). The production of NO_3^- due to nitrification of NH_4^+ in the oxic zone of burrow walls is commonly observed (Kristensen, Jensen, and Andersen 1985). Net NO_3^- fluxes are the results of the balance between nitrification and denitrification, two processes that are tightly coupled in sediments. The coupling between burrow wall nitrification and denitrification in the anoxic regions surrounding burrows can result in strong density dependence of net NO_3^- fluxes and denitrification (Aller 1988; Gilbert, Aller, and Hulth 2003; Braeckman et al. 2010). At high burrow densities (M and S aquaria) showing more complex burrows network (A_{bw}/V_{burrow}; see Fig. 13 and Table 2), the oxic zones surrounding burrows can meld together and, in the extreme, produce virtually continuous oxic conditions that inhibit

denitrification between burrows. Thus in the simplest case the system takes on properties of a deposit with a 1-D diffusion-reaction distribution having a thick oxic zone overlying anoxic sediment and minimized denitrification. It is not simply the fraction of oxidized sediment per volume, but its geometrical distribution that is critical to reactive element fluxes. At low densities, the system is also dominated by 1-D diffusion-reaction patterns, with a relatively thin surface oxic zone, and denitrification is again minimized. Theoretically, for a particular remineralization rate, there are optimal packing patterns of oxic–anoxic microzones at intermediate densities that maximize the proportion of remineralized N that is denitrified. The experimental data here confirm these predicted density dependent patterns directly and also demonstrate, that a single species can have very different net effects on N redox reaction coupling as a function of age-dependent size and population density.

5. Conclusions

Age-specific size classes of a single infaunal species, in this case *Nephtys incisa*, can have different effects on biogenic structure of sediment as a function of size and abundance when present at similar biomass or biovolume in a deposit. Despite qualitative and quantitative differences in burrowing patterns related to size and population abundance, the nonlocal transport coefficients of nonreactive solutes such as Br^- and their resulting net fluxes show little difference. The averaged pore water distributions of TCO_2 and NH_4^+ differ spatially as a function of the *Nephtys* population size and abundance patterns, and averaged depth distributions are well simulated by the nonlocal transport processes parameterized by Br^-. The transport of TCO_2 and NH_4^+ required to account for spatially averaged pore water profiles, however, require attenuations with depth, that reflect differences in the overall time scales governing the distributions of Br^-, averaged distributions of TCO_2 and NH_4^+, and remineralization rates.

At equivalent total biovolume (and biomass), we conclude that burrow density and radius, which depend on the body size structure, directly affect burrow complexity, the extension of surface area and burrow volumes within sediments, and the associated biogeochemical spatial micro-heterogeneity. In sharp contrast to the behavior of nonreactive Br^-, the O_2, TCO_2 and NO_3^- fluxes showed differences as a function of specific burrowing and oxidation patterns, and are thus strongly affected by age-specific population properties of single species. We show that with respect to solute transport, population abundance at a fixed biovolume, and associated burrow habit and oxic sediment volume are the most critical factors. Similar magnitudes of nonlocal transport estimated from nonreactive solutes can be a misleading indicator of the effects of bioturbation activity on benthic biogeochemical cycling.

Because burrowing patterns by *Nephtys incisa* change during its life cycle, our study shows that the impact of a species can differ substantially as a function of size and abundance, and thus consideration must be given to age-specific size–abundance relations and burrowing patterns rather than biovolume–biomass per se.

Acknowledgments. This study was in part funded by the US National Science Foundation (grants OCE0526410 and OCE1332418). It was initially carried out when E. Michaud was a research associate at Stony Brook University in 2007–2008 and continued when R. C. Aller was invited professor at the Université de Bretagne Occidentale in 2014. We thank the R/V *Seawolf* crew and A. Kaushik, N. Protopopescu, and J. Hao for their assistance in the field, I. Klingensmith and J. Y. Aller for assistance in the lab, and M. Sourisseau for his great and precious help for the image processing with Matlab. The authors thank Filip Meysman for having provided both editorial handling and constructive reviews of the manuscript. This is Nereis Park contribution number 32.

REFERENCES

Aller, R. C. 1978. Experimental studies of changes produced by deposit feeders on pore water, sediment, and overlying water chemistry. Amer. J. Sci., *278(9)*, 1185–1234. https://doi.org/10.2475/ajs.278.9.1185

Aller, R. C. 1980. Quantifying solute distributions in the bioturbated zone of marine sediments by defining an average microenvironment. Geochim. Cosmochim. Acta, *44(12)*, 1955–1965. https://doi.org/10.1016/0016-7037(80)90195-7

Aller, R. C. 1982. The effects of macrobenthos on chemical properties of marine sediment and overlying water *in* Animal-Sediment Relations: The Biogenic Alteration of Sediments (Vol. 100). P. L. McCall and M. J. S. Tevesz, eds. Topics in Geobiology. Boston, MA: Springer, pp. 53–102. https://doi.org/10.1007/978-1-4757-1317-6_2

Aller, R. C. 1988. Benthic fauna and biogeochemical processes in marine sediments: The role of burrow structures *in* Nitrogen Cycling in Coastal Marine Environments. T. H. Blackburn and J. Sörensen, eds. New York: John Wiley, pp. 301–338.

Aller, R. C. 2001. Transport and reactions in the bioirrigated zone *in* The Benthic Boundary Layer: Transport Processes and Biogeochemistry. B. P. Boudreau and B. B, Jørgensen, eds. Oxford Press, pp. 269–301.

Aller, R. C., and J. Y. Aller. 1992. Meiofauna and solute transport in marine muds. Limnol. Oceanogr., *37(5)*, 1018–1033. https://doi.org/10.4319/lo.1992.37.5.1018

Aller, R. C., J. Y. Aller, Q. Z. Zhu, C. Heilbrun, I. Klingensmith, and A. Kaushik. 2019. Worm tubes as conduits for the electrogenic microbial grid in marine sediments. Sci. Adv., *5(7)*, Article eaaw3651. https://doi.org/10.1126/sciadv.aaw3651

Aller, R.C., and J. Y. Yingst. 1980. Relationships between microbial distributions and the anaerobic decomposition of organic matter in surface sediments of Long Island Sound, USA. Mar. Biol., *56(1)*, 29–42. https://doi.org/10.1007/BF00390591

Aller, R.C., and J. Y. Yingst. 1985. Effects of the marine deposit-feeders *Heteromastus filiformis* (Polychaeta), *Macoma balthica* (Bivalvia), and *Tellina texana* (Bivalvia) on averaged sedimentary solute transport, reaction rates, and microbial distributions. J. Mar. Res., *43(3),* 615–645. https://doi.org/10.1357/002224085788440349

Anderson, M. J. 2017. Permutational multivariate analysis of variance (permanova) *in* Wiley StatsRef: Statistics Reference Online. N. Balakrishnan, T. Colton, B. Everitt, W. Piegorsch, F. Ruggeri and J. L. Teugels, eds. Accessed 8 November 2021. https://doi.org/10.1002/9781118445112.stat07841

Berger, W. H., A. A. Ekdale, and P. P. Bryant. 1979. Selective preservation of burrows in deep-sea carbonates. Mar. Geol., *32(3)*, 205–230. https://doi.org/10.1016/0025-3227(79)90065-3

Berner, R. A. 1976. Inclusion of adsorption in the modelling of early diagenesis. Earth Planet. Sci. Lett., *29(2)*, 333–340. https://doi.org/10.1016/0012-821X(76)90137-0

Boudreau, B. P. 1984. On the equivalence of nonlocal and radial-diffusion models for porewater irrigation. J. Mar. Res., *42(3)*, 731–735. https://doi.org/10.1357/002224084788505924

Boudreau, B. P. 1997. Diagenetic models and their implementation: Modelling transport and reactions in aquatic sediments. Berlin: Springer. Accessed 8 November 2021. https://catalog.hathitrust.org/api/volumes/oclc/35095947.html

Braeckman, U., M. Y. Foshtomi, D. Van Gansbeke, F. Meysman, K. Soetaert, M. Vincx, and J. Vanaverbeke. 2014. Variable importance of macrofaunal functional biodiversity for biogeochemical cycling in temperate coastal sediments. Ecosystems, *17(4)*,720–737. https://doi.org/10.1007/s10021-014-9755-7

Braeckman, U., P. Provoost, B. Gribsholt, D. V. Gansbeke, J. J. Middelburg, K. Soetaert, M. Vincx, and J. Vanaverbeke. 2010. Role of macrofauna functional traits and density in biogeochemical fluxes and bioturbation. Mar. Ecol. Prog. Ser., *399*, 173–186. https://doi.org/10.3354/meps08336

Buatois, L. A., J. Almond, M. G. Mángano, S. Jensen, and G. J. B. Germs. 2018. Sediment disturbance by Ediacaran bulldozers and the roots of the Cambrian explosion. Sci. Rep., *8(1)*, 4514. https://doi.org/10.1038/s41598-018-22859-9

Burdige, D. J. 2006. Geochemistry of marine sediments. Princeton University Press, 624 pp. https://doi.org/10.1515/9780691216096

Canfield, D. E., and J. Farquhar. 2009. Animal evolution, bioturbation, and the sulfate concentration of the oceans. Proc. Nat. Acad. Sci., *106(20)*, 8123–8127. https://doi.org/10.1073/pnas.0902037106

Chan, B. K. K., K. K. Y. Chan, and P. C. M. Leung. 2006. Burrow architecture of the ghost crab *Ocypode ceratophthalma* on a sandy shore in Hong Kong. Hydrobiologia, *560(1),* 43–49. https://doi.org/10.1007/s10750-005-1088-2

Crane, R. L., and R. A. Merz. 2017. Mechanical properties of sediment determine burrowing success and influence distribution of two lugworm species. J. Exp. Biol., *220(18)*, 3248–3259. https://doi.org/10.1242/jeb.156760

D'Andrea, A. F., and T. H. DeWitt. 2009. Geochemical ecosystem engineering by the mud shrimp *Upogebia pugettensis* (Crustacea: Thalassinidae) in Yaquina Bay, Oregon: Density-dependent effects on organic matter remineralization and nutrient cycling. Limnol. Oceanogr., *54(6)*, 1911–1932. https://doi.org/10.4319/lo.2009.54.6.1911

De Backer, A., F. Van Coillie, F. Montserrat, P. Provoost, C. Van Colen, M. Vincx, and S. Degraer. 2011. Bioturbation effects of *Corophium volutator*: Importance of density and behavioural activity. Estuar. Coastal Shelf Sci., *91(2)*, 306–313. https://doi.org/10.1016/j.ecss.2010.10.031

Dickson, A. G., and F. J. Millero. 1987. A comparison of the equilibrium constants for the dissociation of carbonic acid in seawater media. Deep Sea Res. A, Oceanogr. Res. Pap., *34(10)*, 1733–1743. https://doi.org/10.1016/0198-0149(87)90021-5

Dorgan, K. M. 2015. The biomechanics of burrowing and boring. J. Exp. Biol., *218(2)*, 176–183. https://doi.org/10.1242/jeb.086983

Dornhoffer, T., G. G. Waldbusser, and C. Meile. 2012. Burrow patchiness and oxygen fluxes in bioirrigated sediments. J. Exp. Mar. Biol. Ecol., *412*, 81–86. https://doi.org/10.1016/j.jembe.2011.11.004

Dunn, R. J. K., D. T. Welsh, M. A. Jordan, P. R. Teasdale, and C. J. Lemckert. 2009. Influence of natural amphipod (*Victoriopisa australiensis*) (Chilton, 1923) population densities on benthic metabolism, nutrient fluxes, denitrification and DNRA in sub-tropical estuarine sediment. Hydrobiologia, *628(1)*, 95–109. https://doi.org/10.1007/s10750-009-9748-2

Emerson, S., V. Grundmanis, and D. Graham. 1982. Carbonate chemistry in marine pore waters: MANOP sites C and S. Earth Planet. Sci. Lett., *61(2)*, 220–232. https://doi.org/10.1016/0012-821X(82)90055-3

Emerson, S., R. Jahnke, and D. Heggie. 1984. Sediment-water exchange in shallow water estuarine sediments. J. Mar. Res., *42(3)*, 709–730. https://doi.org/10.1357/002224084788505942

Emmerson, M. C., and D. Raffaelli. 2000. Detecting the effects of diversity on measures of ecosystem function: Experimental design, null models and empirical observations. Oikos, *91(1)*, 195–203. https://doi.org/10.1034/j.1600-0706.2000.910119.x

Gerino, M. 1992. Etude expérimentale de la bioturbation en milieux littoral et profond: Quantification des structures de bioturbation et modélisation du remaniement biologique du sédiment. Thesis, Faculty des sciences, Universite d'Aix-Marseille II. https://www.theses.fr/1992AIX22057

Gilbert, F., R. C. Aller, and S. Hulth. 2003. The influence of macrofaunal burrow spacing and diffusive scaling on sedimentary nitrification and denitrification: An experimental simulation and model approach. J. Mar. Res., *61(1)*, 101–125. https://doi.org/info:doi/10.1357/002224003321586426

Gilbert, F., S. Hulth, V. Grossi, J. C. Poggiale, Gaston Desrosiers, R. Rosenberg, M. Gérino, F. François-Carcaillet, E. Michaud, and G. Stora. 2007. Sediment reworking by marine benthic species from the Gullmar Fjord (western Sweden): Importance of faunal biovolume. J. Exp. Mar. Biol. Ecol., *348(1–2)*, 133–144. https://doi.org/10.1016/j.jembe.2007.04.015

Glud, R. N., N. B. Ramsing, J. K. Gundersen, and I. Klimant. 1996. Planar optrodes: A new tool for fine scale measurements of two-dimensional O_2 distribution in benthic communities. Mar. Ecol. Prog. Ser., *140*, 217–226. https://doi.org/10.3354/meps140217

Goto, K., T. Komatsu, and T. Furukawa. 1962. Rapid colorimetric determination of manganese in waters containing iron: A modification of the formaldoxime method. Anal. Chim. Acta, *27*, 331–334. https://doi.org/10.1016/S0003-2670(00)88510-4

Green, M. A., R. C. Aller, and J. Y. Aller. 1992. Experimental evaluation of the influences of biogenic reworking on carbonate preservation in nearshore sediments. Mar. Geol., *107(3)*, 175–181. https://doi.org/10.1016/0025-3227(92)90166-F

Hale, R., M. N. Mavrogordato, T. J. Tolhurst, and M. Solan. 2014. Characterizations of how species mediate ecosystem properties require more comprehensive functional effect descriptors. Sci. Rep., *4*, Article 6463, 1–6. https://doi.org/10.1038/srep06463

Hall, P. O. J., and R. C. Aller. 1992. Rapid, small-volume, flow injection analysis for SCO2, and NH4+ in marine and freshwaters. Limnol. Oceanogr., *37(5)*, 1113–1119. https://doi.org/10.4319/lo.1992.37.5.1113

Hall, P. O. J., S. Hulth, G. Hulthe, A. Landén, and A. Tengberg. 1996. Benthic nutrient fluxes on a basin-wide scale in the Skagerrak (north-eastern North Sea). J. Sea Res., *35(1–3)*, 123–137. https://doi.org/10.1016/S1385-1101(96)90741-8

Heilskov, A. C., and M. Holmer. 2001. Effects of benthic fauna on organic matter mineralization in fish-farm sediments: Importance of size and abundance. ICES J. Mar. Sci., *58(2)*, 427–434. https://doi.org/10.1006/jmsc.2000.1026

Katrak, G., S. Dittmann, and L. Seuront. 2008. Spatial variation in burrow morphology of the mud shore crab *Helograpsus haswellianus* (Brachyura, Grapsidae) in South Australian saltmarshes. Mar. Fresh. Res., *59(10)*, 902–911. https://doi.org/10.1071/MF08044

Kauppi, L., G. Bernard, R. Bastrop, A. Norkko, and J. Norkko. 2018. Increasing densities of an invasive polychaete enhance bioturbation with variable effects on solute fluxes. Sci. Rep., *8*, Article 7619. https://doi.org/10.1038/s41598-018-25989-2

Kristensen, E., M. J. Jensen, and T. K. Andersen. 1985. The impact of polychaete (*Nereis virens* Sars) burrows on nitrification and nitrate reduction in estuarine sediments. J. Exp. Mar. Biol. Ecol., *85(1)*, 75–91. https://doi.org/10.1016/0022-0981(85)90015-2

Kristensen, E., and J. E. Kostka. 2005. Macrofaunal burrows and irrigation in marine sediment: Microbiological and biogeochemical interactions *in* Interactions Between Macro- and Microorganisms in Marine Sediments. Washington, DC: American Geophysical Union, pp. 125–157.

Lê, S., J. Josse, and F. Husson. 2008. FactoMineR: An R package for multivariate analysis. J. Stat. Software, *25(1)*, 1–18. https://doi.org/10.18637/jss.v025.i01

Lepore, B. J., and P. Barak. 2009. A colorimetric microwell method for determining bromide concentrations. Soil Sci. Soc. Amer. J., *73(4)*, 1130–1136. https://doi.org/10.2136/sssaj2007.0226

Lewis, E. R., and D. W. R. Wallace. 1998. Program Developed for CO_2 System Calculations(CDIAC), CDIAC-105.xml. Environmental System Science Data Infrastructure for a Virtual Ecosystem (ESS-DIVE). https://doi.org/10.15485/1464255

Mackin, J. E., and R. C. Aller. 1984. Ammonium adsorption in marine sediments. Limnol. Oceanogr., *29(2)*, 250–257. https://doi.org/10.4319/lo.1984.29.2.0250

Malkin, S. Y., A. M. F. Rao, D. Seitaj, D. Vasquez-Cardenas, E.-M. Zetsche, S. Hidalgo-Martinez, H. T. S. Boschker, and F. J. R. Meysman. 2014. Natural occurrence of microbial sulphur oxidation by long-range electron transport in the seafloor. ISME J. *8*, 1843–1854. https://doi.org/10.1038/ismej.2014.41

Marinelli, R. L. 1992. Effects of polychaetes on silicate dynamics and fluxes in sediments: Importance of species, animal activity and polychaete effects on benthic diatoms. J. Mar. Res., *50(4)*, 745–779. https://doi.org/10.1357/002224092784797566

Marinelli, R. L., and T. J. Williams. 2003. Evidence for density-dependent effects of infauna on sediment biogeochemistry and benthic–pelagic coupling in nearshore systems. Estuar. Coastal Shelf Sci., *57(1–2)*, 179–192. https://doi.org/10.1016/S0272-7714(02)00342-6

Martin, W. R., and G. T. Banta. 1992. The measurement of sediment irrigation rates: A comparison of the Br^- tracer and $^{222}Rn/^{226}Ra$ disequilibrium techniques. J. Mar. Res., *50(1)*, 125–154. https://doi.org/10.1357/002224092784797737

Mehrbach, C., C. H. Culberson, J. E. Hawley, and R. M. Pytkowicx. 1973. Measurement of the apparent dissociation constants of carbonic acid in seawater at atmospheric pressure. Limnol. Oceanogr., *18(6)*, 897–907. https://doi.org/10.4319/lo.1973.18.6.0897

Meile, C., P. Berg, P. Van Cappellen, and K. Tuncay. 2005. Solute-specific pore water irrigation: Implications for chemical cycling in early diagenesis. J. Mar. Res., *63(3)*, 601–621. https://doi.org/info:doi/10.1357/0022240054307885

Mermillod-Blondin, F., R. Rosenberg, F. François-Carcaillet, K. Norling, and L. Mauclaire. 2004. Influence of bioturbation by three benthic infaunal species on microbial communities and biogeochemical processes in marine sediment. Aquat. Microb. Ecol., *36(3)*, 271–284. https://doi.org/10.3354/ame036271

Meysman, F. J. R. 2018. Cable bacteria take a new breath using long-distance electricity. Trends Microbiol., *26(5)*, 411–422. https://doi.org/10.1016/j.tim.2017.10.011

Meysman, F. J. R., O. S. Galaktionov, R. N. Glud, and J. J. Middelburg. 2010. Oxygen penetration around burrows and roots in aquatic sediments. J. Mar. Res., *68(2)*, 309–336. https://doi.org/10.1357/002224010793721406

Meysman, F. J. R., J. J. Middelburg, and Carlo H. R. Heip. 2006. Bioturbation: A fresh look at Darwin's last idea. Trends Ecol. Evol., *21(12)*, 688–695. https://doi.org/10.1016/j.tree.2006.08.002

Meysman, F. J. R., N. Risgaard-Petersen, S. Y. Malkin, and L. P. Nielsen. 2015. The geochemical fingerprint of microbial long-distance electron transport in the seafloor. Geochim. Cosmochim. Acta, *152*, 122–142. https://doi.org/10.1016/j.gca.2014.12.014

Michaud, E., R. C. Aller, and G. Stora. 2010. Sedimentary organic matter distributions, burrowing activity, and biogeochemical cycling: Natural patterns and experimental artifacts. Estuar. Coastal Shelf Sci., *90(1)*, 21–34. https://doi.org/10.1016/j.ecss.2010.08.005

Michaud, E., G. Desrosiers, R. C. Aller, F. Mermillod-Blondin, B. Sundby, and G. Stora. 2009. Spatial interactions in the *Macoma balthica* community control biogeochemical fluxes at the sediment-water interface and microbial abundances. J. Mar. Res., *67(1)*, 43–70. https://doi.org/info:doi/10.1357/002224009788597926

Michaud, E., G. Desrosiers, F. Mermillod-Blondin, B. Sundby, and G. Stora. 2005. The functional group approach to bioturbation: The effects of biodiffusers and gallery-diffusers of the *Macoma balthica* community on sediment oxygen uptake. J. Exp. Mar. Biol. Ecol., *326(1)*, 77–88. https://doi.org/10.1016/j.jembe.2005.05.016

Miron, G., G. Desrosiers, C. Retière, and R. Lambert. 1991. Évolution spatio-temporelle du réseau de galeries chez le polychète *Nereis virens* (Sars) en relation avec la densité. Canad. J. Zool., *69(1)*, 39–42. https://doi.org/10.1139/z91-006

Murray, F., A. Douglas, and M. Solan. 2014. Species that share traits do not necessarily form distinct and universally applicable functional effect groups. Mar. Ecol. Prog. Ser., *516*, 23–34. https://doi.org/10.3354/meps11020

Needham, H. R., C. A. Pilditch, A. M. Lohrer, and S. F. Thrush. 2010. Habitat dependence in the functional traits of *Austrohelice crassa*, a key bioturbating species. Mar. Ecol. Prog. Ser., *414*, 179–193. https://doi.org/10.3354/meps08726

Nielsen, L. P., and Nils Risgaard-Petersen. 2015. Rethinking sediment biogeochemistry after the discovery of electric currents. Annu. Rev. Mar. Sci., *7(1)*, 425–442. https://doi.org/10.1146/annurev-marine-010814-015708

Norling, K., R. Rosenberg, S. Hulth, A. Grémare, and E. Bonsdorff. 2007. Importance of functional biodiversity and species-specific traits of benthic fauna for ecosystem functions in marine sediment. Mar. Ecol. Prog. Ser., *332*, 11–23. https://doi.org/10.3354/meps332011

Oksanen, J., F. G. Blanchet, M. Friendly, R. Kindt, P. Legendre, D. McGlinn, P. R. Minchin, et al. 2020. Vegan: Community Ecology Package, Version 2.5-7. https://CRAN.R-project.org/package=vegan

Piot, A., C. Nozais, and P. Archambault. 2014. Meiofauna affect the macrobenthic biodiversity–ecosystem functioning relationship. Oikos, *123(2)*, 203–213. https://doi.org/10.1111/j.1600-0706.2013.00631.x

Pischedda, L., P. Cuny, J. L. Esteves, J.-C. Poggiale, and F. Gilbert. 2012. Spatial oxygen heterogeneity in a *Hediste diversicolor* irrigated burrow. Hydrobiologia, *680(1)*, 109–124. https://doi.org/10.1007/s10750-011-0907-x

Pischedda, L., J.-C. Poggiale, P. Cuny, and F. Gilbert. 2008. Imaging oxygen distribution in marine sediments. The importance of bioturbation and sediment heterogeneity. Acta Biotheoret., *56(1)*, 123–135. https://doi.org/10.1007/s10441-008-9033-1

Presley, B. J. 1971. Appendix: Techniques for analyzing interstitial water samples. Part 1: Determination of selected minor and major inorganic constituents *in* Initial Reports of the Deep Sea Drilling Project. Washington, DC.: U.S. Government Printing Office. Accessed 8 November 2021. http://www.deepseadrilling.org/07/volume/dsdp07pt2_appendixI.pdf

Quintana, C. O., M. Shimabukuro, C. O. Pereira, B. G. R. Alves, P. C. Moraes, T. Valdemarsen, E. Kristensen, and P. Y. G. Sumida. 2015. Carbon mineralization pathways and bioturbation in coastal Brazilian sediments. Sci. Rep., *5*, Article 16122. https://doi.org/10.1038/srep16122

R Core Team. 2021. R: A language and environment for statistical computing. Vienna: R Foundation for Statistical Computing. https://www.R-project.org

Rao, A. M. F., S. Y. Malkin, F. Montserrat, and F. J. R. Meysman. 2014. Alkalinity production in intertidal sands intensified by lugworm bioirrigation. Estuar. Coastal Shelf Sci., *148*, 36–47. https://doi.org/10.1016/j.ecss.2014.06.006

Rhoads, D.C. 1974. Organism sediment relations on the muddy sea floor. Oceanogr. Mar. Biol. Annu. Rev., *12*, 263–300.

Robbins, L. L., M. E. Hansen, J. A. Kleypas, and S. C. Meylan. 2010. CO_2calc: A user-friendly seawater carbon calculator for Windows, Max OS X, and IOS (iPhone): Open-file report 2010–1280. St. Petersburg, FL: US Geological Survey, 17 pp. https://pubs.usgs.gov/of/2010/1280/

Rosenfeld, J. K. 1979. Ammonium adsorption in nearshore anoxic sediments. Limnol. Oceanogr., *24(2)*, 356–364. https://doi.org/10.4319/lo.1979.24.2.0356

Schink, J. C, J. H. Stockwell, and R. A. Ellis. 1979. An improved device for gasometric determination of carbonate in sediment. J. Sediment. Res., *49(2)*, 651–653. https://doi.org/10.1306/212F77ED-2B24-11D7-8648000102C1865D

Shumway, S. E. 1979. The effects of body size, oxygen tension and mode of life on the oxygen uptake rates of polychaetes. Compar. Biochem. Physiol. A, Physiol., *64(2)*, 273–278. https://doi.org/10.1016/0300-9629(79)90660-1

Solan, M., B. J. Cardinale, A. L. Downing, K. A. M. Engelhardt, J. L. Ruesink, and D. S. Srivastava. 2004. Extinction and ecosystem function in the marine benthos. Science, *306(5699)*, 1177–1180. https://doi.org/10.1126/science.1103960

Solórzano, L. 1969. Determination of ammonia in natural waters by the phenolhypochlorite method. Limnol. Oceanogr., *14(5)*, 799–801. https://doi.org/10.4319/lo.1969.14.5.0799

Stookey, L. L. 1970. Ferrozine—A new spectrophotometric reagent for iron. Anal. Chem., *42(7)*, 779–781. https://doi.org/10.1021/ac60289a016

Thayer, C. W. 1979. Biological bulldozers and the evolution of marine benthic communities. Science, *203(4379)*, 458–461. https://doi.org/10.1126/science.203.4379.458

Trevor, J. H. 1976. The burrowing activity of *Nephtys cirrosa* Ehlers (Annelida: Polychaeta). J. Exp. Mar. Biol. Ecol., *24(3)*, 307–319. https://doi.org/10.1016/0022-0981(76)90062-9

Trevor, J. H. 1978. The dynamics and mechanical energy expenditure of the polychaetes *Nephtys cirrosa*, *Nereis diversicolor* and *Arenicola marina* during burrowing. Estuar. Coastal Mar. Sci., *6(6)*, 605–619. https://doi.org/10.1016/0302-3524(78)90034-8

Waldbusser, G. G., and R. L. Marinelli. 2006. Macrofaunal modification of porewater advection: Role of species function, species interaction, and kinetics. Mar. Ecol. Prog. Ser., *311*, 217–231. https://doi.org/10.3354/meps311217

Waldbusser, G. G., R. L. Marinelli, R. B. Whitlatch, and P. T. Visscher. 2004. The effects of infaunal biodiversity on biogeochemistry of coastal marine sediments. Limnol. Oceanogr., *49(5)*, 1482–1492. https://doi.org/10.4319/lo.2004.49.5.1482

Wenzhöfer, F., and R. N. Glud. 2004. Small-scale spatial and temporal variability in coastal benthic O_2 dynamics: Effects of fauna activity. Limnol. Oceanogr., *49(5)*, 1471–1481.

Westrich, J. T., and R. A. Berner. 1984. The role of sedimentary organic matter in bacterial sulfate reduction: The *G* model tested. Limnol. Oceanogr., *29(2)*, 236–249. https://doi.org/10.4319/lo.1984.29.2.0236

Westrich, J. T., and R. A. Berner. 1988. The effect of temperature on rates of sulfate reduction in marine sediments. Geomicrobiol. J., *6(2)*, 99–117. https://doi.org/10.1080/01490458809377828

Whitlatch, R. B. 1976. Seasonality, species diversity, and patterns of resource utilization in a marine deposit-feeding community. Ph.D. diss., University of Chicago.

Yin, H., R. C. Aller, Q. Zhu, and J.Y. Aller. 2021. The dynamics of cable bacteria colonization in surface sediments: A 2D view. Sci. Rep. *11*, 7167. https://doi.org/10.1038/s41598-021-86365-1

Zajac, R. N., and R. B. Whitlatch. 1988. Population ecology of the polychaete *Nephtys incisa* in Long Island Sound and the effects of disturbance. Estuaries, *11(2)*, 117–133. https://doi.org/10.2307/1351999

Zhu, Q. Z., R. C. Aller, and Y. Fan. 2005. High-performance planar pH fluorosensor for two-dimensional pH measurements in marine sediment and water. Environ. Sci. Tech., *39(22)*, 8906–8911. https://doi.org/10.1021/es051023m

Zhu, Q. Z., R. C. Aller, and Y. Fan. 2006a. A new ratiometric, planar fluorosensor for measuring high resolution, two-dimensional pCO_2 distributions in marine sediments. Mar. Chem., *101(1–2)*, 40–53. https://doi.org/10.1016/j.marchem.2006.01.002

Zhu, Q. Z., R. C. Aller, and Y. Fan. 2006b. Two-dimensional pH distributions and dynamics in bioturbated marine sediments. Geochim. Cosmochim. Acta, *70(19)*, 4933–4949. https://doi.org/10.1016/j.gca.2006.07.033

Received: *12 July 2021*; revised: *5 September 2021*.